The constancy of galactic cosmic rays as recorded by cosmogenic nuclides in iron meteorites

Thomas SMITH[1,4], David L. COOK [iD][2], Silke MERCHEL[3], Stefan PAVETICH[3,5], Georg RUGEL[3], Andreas SCHARF[3], and Ingo LEYA [iD][1*]

[1]Physics Institute, University of Bern, Sidlerstrasse 5, CH-3012 Bern, Switzerland
[2]Institute for Geochemistry and Petrology, ETH Zürich, Clausiusstrasse 25, 8092 Zürich, Switzerland
[3]Helmholtz-Zentrum Dresden-Rossendorf, Bautzner Landstrasse 400, 01328 Dresden, Germany
[4]Present address: Institute of Geology and Geophysics, Chinese Academy of Sciences, 19 Beitucheng Western Road, Box 9825, 100029 Beijing, People's Republic of China
[5]Present address: Department of Nuclear Physics, Research School of Physics and Engineering, The Australian National University, Canberra, ACT 2601, Australia
[*]Corresponding author. E-mail: Ingo.leya@space.unibe.ch

Abstract–We measured the He, Ne, and Ar isotopic concentrations and the ^{10}Be, ^{26}Al, ^{36}Cl, and ^{41}Ca concentrations in 56 iron meteorites of groups IIIAB, IIAB, IVA, IC, IIA, IIB, and one ungrouped. From ^{41}Ca and ^{36}Cl data, we calculated terrestrial ages indistinguishable from zero for six samples, indicating recent falls, up to 562 ± 86 ka. Three of the studied meteorites are falls. The data for the other 47 irons confirm that terrestrial ages for iron meteorites can be as long as a few hundred thousand years even in relatively humid conditions. The ^{36}Cl-^{36}Ar cosmic ray exposure (CRE) ages range from 4.3 ± 0.4 Ma to 652 ± 99 Ma. By including literature data, we established a consistent and reliable CRE age database for 67 iron meteorites. The high quality of the CRE ages enables us to study structures in the CRE age histogram more reliably. At first sight, the CRE age histogram shows peaks at about 400 and 630 Ma. After correction for pairing, the updated CRE age histogram comprises 41 individual samples and shows no indications of temporal periodicity, especially not if one considers each iron meteorite group separately. Our study contradicts the hypothesis of periodic GCR intensity variations (Shaviv 2002, 2003), confirming other studies indicating that there are no periodic structures in the CRE age histogram (e.g., Rahmstorf et al. 2004; Jahnke 2005). The data contradict the hypothesis that periodic GCR intensity variations might have triggered periodic Earth climate changes. The ^{36}Cl-^{36}Ar CRE ages are on average 40% lower than the ^{41}K-K CRE ages (e.g., Voshage 1967). This offset can either be due to an offset in the ^{41}K-K dating system or due to a significantly lower GCR intensity in the time interval 195–656 Ma compared to the recent past. A 40% lower GCR intensity, however, would have increased the Earth temperature by up to 2 °C, which seems unrealistic and leaves an ill-defined ^{41}K-K CRE age system the most likely explanation. Finally, we present new ^{26}Al/^{21}Ne and ^{10}Be/^{21}Ne production rate ratios of 0.32 ± 0.01 and 0.44 ± 0.03, respectively.

INTRODUCTION

An important question in climate change studies is the effect of cosmic rays. Svensmark and Friis-Christensen (1997) and Svensmark (1998) claimed that the Earth's cloud cover is correlated with the cosmic ray flux. In these pioneering studies, the authors concluded that about 3–4% of the global cloud cover is correlated with the intensity of cosmic rays, which is itself inversely correlated with solar activity. Their study is based on cloud data from only one solar cycle and they considered only oceanic cloud cover data. Kristjànsson

et al. (2002) added data for a second solar cycle, performed a reevaluation, and found no significant correlation. Later, Laut (2003) argued that the correlations between cloud coverage and the galactic cosmic ray (GCR) flux were obtained erroneously. Kirkby (2007) argued that, although the fundamental physical and chemical processes are not understood, there is a close relationship between GCR variations and climate changes, influencing to some extent cloud coverage, tropical rainfall, and the location of the Intertropical Convergence Zone. Erlykin et al. (2010) argued that there is a negative correlation between GCR intensity and cloud coverage at low altitudes and a positive correlation of solar irradiance with cloud coverage at middle altitudes.

By assuming that there is a causal link between GCR intensity and global warming, Erlykin et al. (2009) determined that the long-term variation is expected to be less than 0.07 °C since 1956, which would be less than 14% of the observed global warming. Other studies have confirmed these results (e.g., Sloan and Wolfendale 2008, 2013a; Sloan 2013). Ormes (2017) on the other hand, concluded that there is no identifiable correlation between cloud coverage and GCR intensity.

Although there is no consensus on a correlation, some studies have continued to assume a relationship between GCR intensity and cloud cover. Frigo et al. (2013) argued for a possible influence of GCRs on climate on a regional scale and Artamonova and Veretenenko (2011) concluded that GCRs may influence the process of cyclone and anticyclone formation.

Shaviv (2002, 2003) proposed that the occurrence of ice-age epochs on the Earth was influenced by the solar system crossing through the spiral-arms of the Milky Way. In the diffusional model of Shaviv, variations in GCR fluence between the regions within and outside of the spiral arms may be up to a factor of three. The GCR flux is higher in galactic spiral arms than in interarm regions due to higher supernova rates and/or closer proximity to supernovae explosions. He proposed, by assuming four galactic spiral-arms for the Milky Way, a spiral crossing period for the solar system of ~140 Ma. Shaviv also argued that this periodicity is seen in the GCR exposure age histogram for iron meteorites. Although some studies were supportive (e.g., Wallmann 2004; Gies and Helsel 2005), many subsequent investigations have questioned the original hypothesis. First, Sloan and Wolfendale (2013b) calculated GCR intensity variations between spiral-arm and interarm regions to be in the range 10–20% and not more than 30%, that is, far less than the factor of three assumed by Shaviv (2002, 2003). In addition, the calculated periodicity depends on the number of galactic

spiral-arms. While there are indeed some arguments that the Milky Way has four spiral-arms (e.g., Vallée 2017), there are also some arguments for a two-armed spiral in the Milky Way (Drimmel 2000). If true, the periodicity of the GCR intensity variations would be closer to 280 Ma and would no longer be in accord with periodic Earth climate changes. Using new data on the structure of the Milky Way, Overholt et al. (2009) argued for a nonsymmetric galaxy and concluded that the timing of the crossing of our solar system through galactic spiral-arms is most likely irregular. A second and motivating rationale for the present study are questions about the interpretation of the meteorite data by Shaviv (2002, 2003). For example, Rahmstorf et al. (2004) argued that Shaviv misinterpreted the iron meteorite data (see also Wieler et al. 2013). Going one step further, Alexeev (2016) used the same data set as Shaviv (2002, 2003) but reinterpreted the data by fully considering uncertainties for the cosmic ray exposure (CRE) ages and using the now accepted chemical grouping for iron meteorites. Doing so, he found no indications for a periodicity of 140 Ma in the CRE age histogram but he found slight indications of a periodicity in the range 400–500 Ma. Jahnke (2005), using the same data set, found no indications for any periodic signal in the CRE age histogram for iron meteorites.

This discussion illustrates the difficulties of studying periodic structures in the CRE age histogram of iron meteorites using existing data, which mainly consist of the ^{41}K-K CRE ages from H. Voshage (e.g., Voshage and Feldmann 1978, 1979). The main reason lies in the sometimes large uncertainties of up to 100 Ma for individual ages. The large uncertainties make it difficult or even impossible to judge whether two meteorites from the same chemical group were produced in the same ejection event. This pairing correction must be applied before the CRE age histogram can be used to identify periodic structures and/or meteorite delivery mechanisms. Any under- or overcorrection for pairing can either produce (apparent) peaks in the CRE age histogram or smear them out. This is the motivation for the present study: to improve the quality of the CRE ages of iron meteorites and to then identify possible structures in the CRE age histogram, if they exist.

THEORETICAL BASICS

Shaviv (2002, 2003) proposed that periodic galactic fluence variations produce peaks in the CRE age histogram for iron meteorites. Wieler et al. (2013) demonstrated that periodic GCR intensity variations produce periodic structures in the CRE age histogram if the meteorite delivery rate is constant. Their theoretical

approach is based on CRE ages calculated via the ^{40}K-K dating system, which is based on a cosmogenic radionuclide with a half-life of 1.251 Ga. For our work, we use the ^{36}Cl-^{36}Ar dating system, which is based on a radionuclide with a half-life of 301,000 years. Figure 1 shows artificial CRE age histograms of ^{36}Cl-^{36}Ar CRE ages for iron meteorites assuming periodic changes in the GCR intensity. The histogram has been constructed as follows: First, the time axis for meteorite production ranging from zero up to 1050 Ma has been divided into 10 Ma bins. For each bin, a nominal GCR fluence has been assigned. For the first 150 Ma, we assigned arbitrary a GCR fluence of 1; for the time interval 150–300 Ma, we assigned a GCR fluence of either 1, 1.5, or 3; for the time interval 300–450 Ma, we again assigned a value of 1, and so on. The upper two panels are for a constant GCR intensity (always 1), the middle two panels are for periodic GCR fluence variations of a factor of 1.5, that is, roughly in accord with the proposal by Sloan and Wolfendale (2013a), and the lower two panels are for periodic GCR fluence variations of a factor of 3, as proposed by Shaviv (2002, 2003). As a period we always use 150 Ma, close to the value proposed by Shaviv (2002, 2003). Second, for each bin, we calculated the total number of cosmogenic ^{36}Ar atoms. For example, for the bin 750–760 Ma, we calculated the total number of ^{36}Ar atoms produced for the entire irradiation of the meteorite, from its production 760 Ma ago up to its fall on the Earth ($T = 0$). By combining the thus calculated ^{36}Ar concentrations with the ^{36}Cl data, which are always for the recent GCR fluence of 1, we then calculated the apparent age of the meteorite, which is higher than the real age due to enhanced production of ^{36}Ar in the time period 150–300 Ma, 450–600 Ma, and 750–760 Ma. In this special example, the real age is 760 Ma and the apparent age is 1380 Ma. Doing this type of calculation for all 10 Ma bins, we then constructed a CRE age histogram for the apparent ages. Note that the real-time axis is always from 0 to 1050 Ma and that the periodic GCR intensity changes are always in the same time intervals, that is, low at 0–150 Ma, 300–450 Ma, 600–750 Ma, and 900–1050 Ma and enhanced at 150–300 Ma, 450–600 Ma, and 750–900 Ma. Therefore, the number of peaks visible in the histograms is always the same, only their magnitude and their period depends on the assumed enhancement of the GCR fluence. For the data shown in the left panels, we assume a constant rate for the production of meteorites and an unchanging probability of transport to and capture by the Earth. For constructing the diagrams in the right panels, we divided the time axis into 10 Ma bins (as for the panels on the left) and we used a random number generator to assign to each bin how many meteorites have been

produced and delivered to the Earth. We do not consider here the expected exponential decease of number of iron meteorites with increasing CRE age, that is, we assume a constant probability of the Earth capture and disregard competing mechanisms for meteoroid destruction (e.g., Alexeev 2016). This assumption does not compromise the following discussion and conclusions. What does affect the CRE age histogram are the assumptions we made concerning uncertainties and bin sizes. For the artificial histograms shown here, we neglect any uncertainties, that is, the ages have an uncertainty of zero. With the assumed flux variations of factors 1.5 and 3.0 and the chosen bin size of 30 Ma, there is no piling up in the histogram, there is only a periodic compression. With larger flux variations, and/or larger bin sizes, and/or including uncertainties, events pile up in the histogram. The histograms are normalized to the same number of meteorites, which explain some of the non-integer numbers in the right hand panels.

There are two important findings; first, periodic GCR fluence variations indeed produce time-dependent structures in the CRE age histogram. This is true for both cases, for constant (left column) and for stochastic (right column) production of iron meteorites. The solid lines indicate the results of a peak search algorithm. Other than the identification of noise, there are no clear indications for periodic structures in the upper two panels (constant GCR). Time-dependent structures are clearly visible for a constant meteorite delivery and ΔGCR = 1.5 (middle left panel). For the case ΔGCR = 1.5 and stochastic meteorite production, there are hints for time-dependent structures, but they are not well constrained. The time-dependent structures become much more robust for ΔGCR = 3.0 (lower panels). Second, the time dependence is not strictly periodic. For example, for ΔGCR = 1.5, the peaks in the CRE age histogram are at 90, 450, 870, and 1190 Ma; the period ranges from 320 to 420 Ma. For periodic GCR intensity changes of ΔGCR = 3.0, the peaks are at 70, 670, 1270, and 1850 Ma; the periodicity is in the range 600 Ma. The periodicity seen in the CRE age histogram not only depends on the period of the GCR fluence change but also on the magnitude of this change. This finding, though never discussed so far, is actually expected; during times of low GCR intensity, the "cosmic ray clock" is running slow, and at times of high GCR intensity, the clock is running fast. Therefore, GCR intensity variations stretch and compress the time-axis in the histogram. The histogram in Fig. 1 is set up in a way that the average GCR fluence used in the upper two panels (GCR constant) corresponds to the lowest fluence assumed for the other two cases with periodic GCR fluence variations. The case ΔGCR = 1.5,
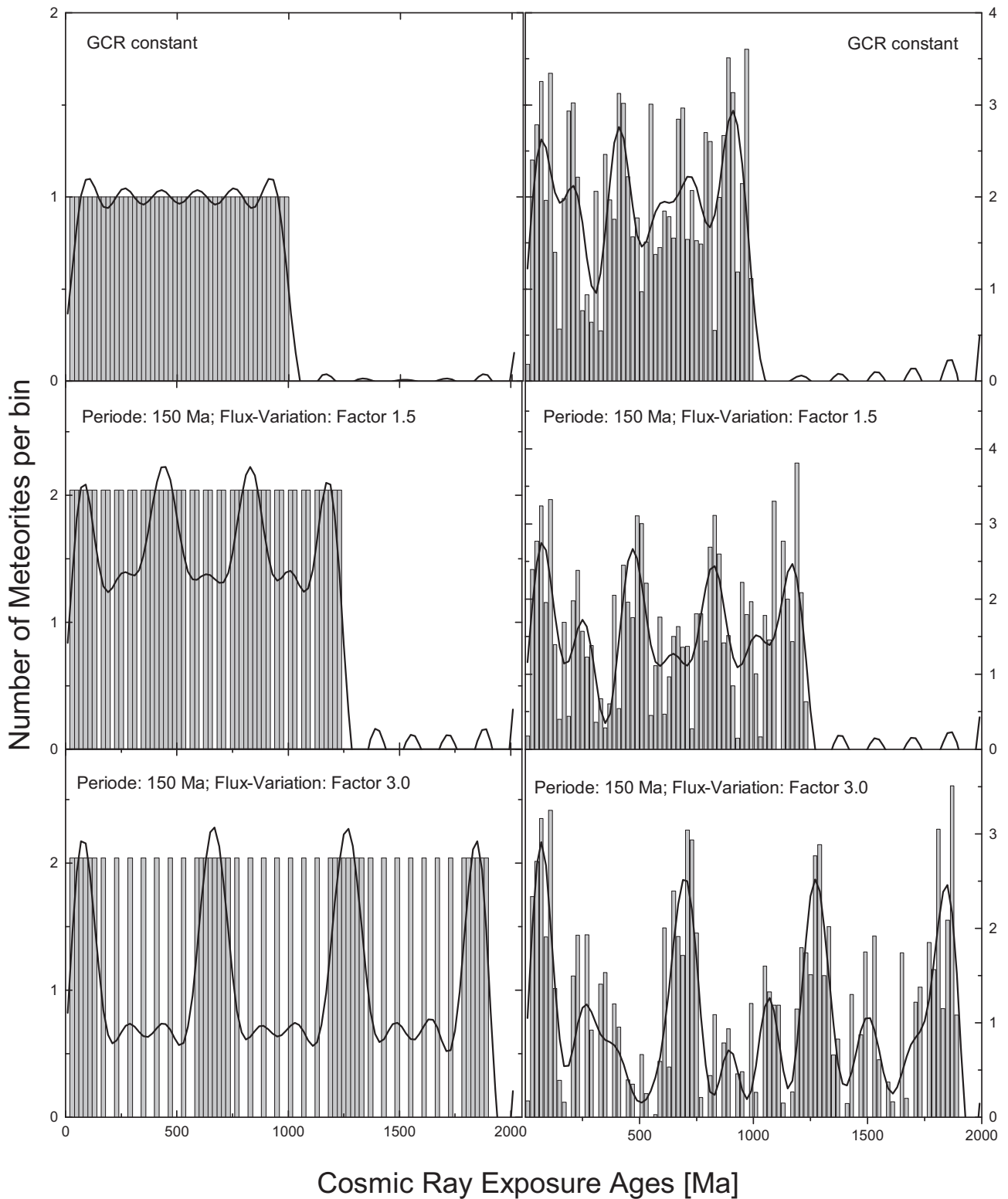
Fig. 1. Modeled cosmic ray exposure age histogram for iron meteorites. The left panels are for constant production of iron meteorites in the asteroid belt. The right panels are for stochastic production of iron meteorites. The upper two panels are for a constant GCR flux, the middle two panels are for GCR flux variations of a factor of 1.5, and the bottom two panels are for GCR flux variations of a factor of 3. The solid line is the result of a simple peak-search algorithm applied to the constructed CRE age histograms. For more information, see text.

therefore, stands for an average GCR fluence at the low end and a 1.5 times higher GCR fluence at the high end. Assuming a periodicity always increases the ages and expands the time-axis in the CRE age histogram. This can also be seen by the finding that for modeling we assume continuous meteorite production from present up to 1 Ga, but the apparent ages, calculated with the periodic GCR fluence variations, range up to 2 Ga, that is, the entire time-axis is stretched.

To summarize, provided that a high quality CRE age histogram for iron meteorites can be established, it would not only be possible to study transit processes for iron meteorites, it would also help answering the question of whether the CRE ages for iron meteorite support the assumption of periodic fluence variations.

EXPERIMENTAL

Samples

We selected a total of 56 iron meteorites from six different groups; 42 are IIIABs, seven are IIABs, three are IVAs, one IC, one IIA, one IIB, and one ungrouped. Table A1 in Appendix A summarizes some of the relevant information: names, source collections, and the total collected mass. All samples were analyzed for the noble gases He, Ne, and Ar and the lighter cosmogenic radionuclides (CRN) ^{10}Be, ^{26}Al, ^{36}Cl, and ^{41}Ca.

The samples were first cut into smaller pieces with masses in the range 60–200 mg. They were cleaned with ethanol to remove any contamination from cutting and were carefully studied under a binocular microscope to check for troilite and schreibersite inclusions. Samples with visible inclusions were not used for further studies. This preselection reduces the problem caused by inclusions (see below); we cannot completely exclude minor inclusions in our samples (see also Ammon et al. 2008).

Noble Gases

The He, Ne, and Ar isotopic concentrations were measured in the noble gas laboratory at the University of Bern. For a detailed description of the procedure used, see Ammon et al. (2008, 2011) and Smith et al. (2017). The samples were loaded into an all-metal (except for a glass window) noble gas extraction line and were preheated in vacuum at ~80 °C for 1–2 days to remove atmospheric surface contamination. The samples were degassed in a Mo crucible held at ~1800 °C for ~30–40 min. A boron-nitride liner inside the Mo crucible prevents corrosion of the latter. We regularly performed second extractions at slightly higher temperatures to check whether the samples have been completely degassed. In addition, we regularly performed blank measurements. Both re-extractions and blanks contributed less than ~1% to the measured sample gas amounts for He and Ne isotopes and less than 10% for Ar isotopes. After extraction, the gases were first cleaned on various getters (SAES®) working in the temperature range between room temperature and 280 °C. Subsequently, an Ar fraction was cryogenically separated from the He–Ne fraction using activated charcoal held at the temperature of boiling liquid nitrogen (LN$_2$). Helium and Ne isotopes were analyzed using an in-house made sector field mass spectrometer. During He and Ne measurements, charcoal (at LN$_2$) was used to reduce interfering species such as Ar, water, and some hydrocarbons. The separated Ar fraction (the same sample) was routed to an in-house made tandem mass spectrometer optimized to reduce baseline variations on ^{36}Ar and especially on ^{38}Ar due to scattered ^{40}Ar ions. All measurements were performed in peak-jumping mode and both spectrometers were regularly calibrated using standard gases. All standard gases are of atmospheric isotopic ratios except for He, which is enriched in ^{3}He relative to air.

Cosmogenic Radionuclides

The procedures used for chemical separation were adopted from those developed earlier by Merchel and Herpers (1999). The measurements were divided into eight batches (excluding one batch for the big iron meteorite Twannberg, cf. Smith et al. 2017), each consists of seven samples and one blank. Meteorite samples with masses ranging from 56 to 214 mg were dissolved in HNO$_3$ (2 M) at room temperature. After adding carrier solutions of natural ^{35}Cl/^{37}Cl, AgCl was precipitated and treated separately in a dedicated ^{36}Cl laboratory for isobar reduction and further cleaning. The remaining sample solution was transferred to a normal laboratory and further stable isotope carriers were added (^{9}Be, ^{27}Al, ^{nat}Ca, ^{55}Mn) to allow chemical separation. To determine the target elements relevant for the production of the cosmogenic nuclides of interest here (Fe and Ni), we took aliquots of 2–3% for inductively coupled plasma mass spectrometry (ICP-MS). For the further separation of Be, Al, Ca, Fe, and Mn fractions, anion and cation exchange and repeated precipitations were performed. The separated fractions were further purified from their respective isobars and finally converted to oxides (BeO, Al$_2$O$_3$, MnO$_2$, Fe$_2$O$_3$) and fluorides (CaF$_2$). The ^{10}Be/^{9}Be, ^{26}Al/^{27}Al, ^{36}Cl/^{35}Cl, and ^{41}Ca/^{40}Ca ratios were measured at the Dresden AMS facility (DREAMS) at the Helmholtz-Zentrum

Dresden-Rossendorf (HZDR, Germany; Akhmadaliev et al. 2013; Pavetich et al. 2016; Rugel et al. 2016).

For normalization, we use the secondary in-house standards "SMD-Be-12," "SMD-Al-11," "SM-Cl-11," and "SMD-Ca-12" for $^{10}Be/^9Be$, $^{26}Al/^{27}Al$, $^{36}Cl/^{35+37}Cl$, and $^{41}Ca/^{40}Ca$, respectively (Merchel et al. 2011; Akhmadaliev et al. 2013; Rugel et al. 2016). The seven samples of each batch were accompanied by one process blank. The average blank ratios are $(4.0 \pm 2.2) \times 10^{-15}$ and $(1.7 \pm 0.7) \times 10^{-14}$ for $^{10}Be/^9Be$ and $^{26}Al/^{27}Al$, respectively, which correspond to blank corrections below 4.7% for $^{10}Be/^9Be$ and 0.7–31% for $^{26}Al/^{27}Al$. For $^{36}Cl/^{35}Cl$ and $^{41}Ca/^{40}Ca$ the average blanks are $(1.4 \pm 0.8) \times 10^{-14}$ and $(7.6 \pm 6.6) \times 10^{-15}$. The $^{41}Ca/^{40}Ca$ blank of the first batch was significantly higher at 2.3 ± 10^{-13}. The average $^{36}Cl/^{35}Cl$ and $^{41}Ca/^{40}Ca$ blanks correspond to corrections in the range of <0.2%, and 1.2–39%, respectively. The chemical yields of the eight batches are (on average) ~85%, ~54%, ~73%, and ~71% for BeO, Al_2O_3, AgCl, and CaF_2, respectively.

From the measured ratios, we calculate the concentrations, in dpm kg^{-1}, using equations of the following type (here the example for ^{10}Be):

$$^{10}Be = \frac{^9Be_{carrier} \times N_A \times R \times \lambda_{10}}{M_{Be} \times m} \left[\frac{dpm}{kg}\right] \quad (1)$$

where $^9Be_{carrier}$ is the amount of ^9Be carrier added (g), R represents the measured $^{10}Be/^9Be$ ratio, N_A is Avogadro's number $(6.02 \times 10^{23} \text{ mol}^{-1})$, λ_{10} is the decay constant of ^{10}Be $([9.50 \pm 0.08] \times 10^{-13} \text{ min}^{-1}$; Korschinek et al. 2010), M_{Be} is the molar mass of Be $(9.012182 \text{ g mol}^{-1})$, and m is the mass of the sample (kg). The decay constants used for ^{26}Al, ^{36}Cl, and ^{41}Ca are $\lambda_{26} = (9.67 \pm 0.32) \times 10^{-7} \text{ yr}^{-1}$, $\lambda_{36} = (2.301 \pm 0.011) \times 10^{-6} \text{ yr}^{-1}$, and $\lambda_{41} = (6.97 \pm 0.11) \times 10^{-6} \text{ yr}^{-1}$, respectively (see also below).

EXPERIMENTAL RESULTS AND DISCUSSION

Noble Gases

Helium

The $^4He/^3He$ ratios and ^3He concentrations are given in Table A2 in Appendix A. We cannot give He data for the meteorites Bristol, Brownfield, Calico Rock, Fort Pierre, Gan Gan, Mapleton, Norfolk, Rowton, Treysa, and Verkhne Udinsk due to technical problems during the measurements. Figure 2 depicts the $^4He/^3He$ ratios, which range between 1.63 ± 0.09 and 12.89 ± 0.73. Thirty-eight of the selected meteorites have $^4He/^3He$ ratios in the range 3–7 (indicated by the

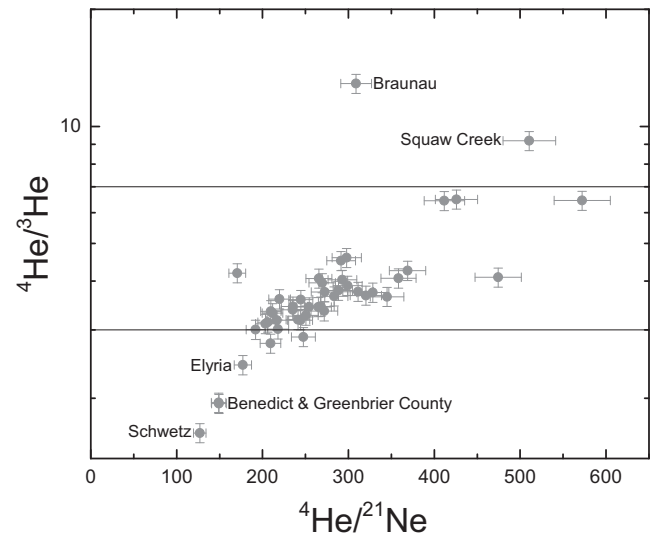Fig. 2. $(^4He/^3He)$ as a function of $(^4He/^{21}Ne)$ for the studied iron meteorites. The two horizontal lines at $(^4He/^3He) = 3$ and 7 define the range of cosmogenic $(^4He/^3He)$ predicted by the model calculations. The six meteorites with too low or too high ratios are labeled.

two horizontal lines in Fig. 2), well within the range expected for cosmogenic production (e.g., Ammon et al. 2009). Four samples have $^4He/^3He$ ratios lower than expected for cosmogenic production and two (Braunau and Squaw Creek) have $^4He/^3He$ ratios of 9.2 and 12.8, that is, significantly higher than cosmogenic. The *higher* $^4He/^3He$ ratios for Braunau and Squaw Creek can either be due to remaining atmospheric contamination $(^4He/^3He \sim 10^6)$ or radiogenic ^4He from decay of uranium and thorium; both are known trace elements in troilite and/or schreibersite inclusions. An additional possibility is the loss of tritium before its decay to ^3He caused by solar heating in orbits close to the sun. Atmospheric ^4He contamination would likely be accompanied by an even more significant ^{40}Ar contamination. The $^{40}Ar/^{36}Ar$ ratios of 143 and 207, respectively, for Braunau and Squaw Creek are relatively high, but they are comparable to ratios of other meteorites. We conclude that atmospheric contamination most likely is not the reason for the high measured $^4He/^3He$ ratios. If the studied samples from Braunau and Squaw Creek were to have been compromised by ^4He from troilite and schreibersite, there would be higher than normal $^{22}Ne/^{21}Ne$ ratios (see below). The measured $^{22}Ne/^{21}Ne$ ratios for both meteorite samples are not exceptionally high. This seemingly leaves ^3He deficits due to tritium loss the most likely explanation. However, there are also convincing arguments against the tritium loss hypothesis. The $^4He_{cos}$ values given for Braunau and

Squaw Creek in Table 1 were calculated using $^4\text{He}_{cos} = {}^3\text{He}_{cos} \times 3.96$, with 3.96 as the average of all measured $^4\text{He}/^3\text{He}$ ratios that are within the predicted range of 3–7. If ^3He would be too low, we would calculate too low $^4\text{He}_{cos}$ values. However, the thus calculated $^4\text{He}_{cos}$ values and with them the $(^4\text{He}/^{21}\text{Ne})_{cos}$ ratios for both meteorites are reasonable, that is, the data for both meteorites fit well into the established correlations between $(^4\text{He}/^{38}\text{Ar})_{cos}$ versus $(^4\text{He}/^{21}\text{Ne})_{cos}$ and ^{10}Be versus $(^4\text{He}/^{21}\text{Ne})_{cos}$ (see below). Consequently, ^3He deficits due to tritium losses are also not a viable explanation for the high $^4\text{He}/^3\text{He}$ ratios. Note that Hampel and Schaeffer (1979) measured in the iron meteorite Braunau a $^4\text{He}/^3\text{He}$ ratio of 10.1, that is, close to the value of 12.9 measured by us. In addition, Lavielle et al. (1995) measured a $^4\text{He}/^3\text{He}$ ratio of about 8 for the Old Woman iron meteorite. While it is already difficult to explain the *high* $^4\text{He}/^3\text{He}$ ratios, we might have an explanation for the *low* $^4\text{He}/^3\text{He}$ ratios measured for four samples. The *low ratios* can either be due to low ^4He or high ^3He concentrations. However, there is no trend that samples with low $^4\text{He}/^3\text{He}$ ratios have high ^3He concentrations. The trend is rather opposite: samples with low $^4\text{He}/^3\text{He}$ ratios have low ^3He and ^4He concentrations. There is, however, a trend that samples with low $^4\text{He}/^3\text{He}$ ratios have low $^4\text{He}/^{21}\text{Ne}$ ratios (see Fig. 2), indicating a small pre-atmospheric radius. Indeed, the recovered masses for the four meteorites in question are less than 21.5 kg (see Table A1 in Appendix A). In Fig. 2, the four meteorites follow the general trend of decreasing $^4\text{He}/^3\text{He}$ with decreasing $^4\text{He}/^{21}\text{Ne}$ ratios. Therefore, there is no reason to doubt the data and the conclusion might be that the model predictions overestimate $^4\text{He}/^3\text{He}$ ratios for small meteorites and/or close to the surface.

Neon

The measured $^{20}\text{Ne}/^{22}\text{Ne}$ and $^{22}\text{Ne}/^{21}\text{Ne}$ ratios and ^{20}Ne gas amounts after correction for fractionation and interferences but before blank correction are given in Table A2 in Appendix A. We decided not to make any blank corrections at this point because the blank is atmospheric and can be best corrected using a two-component deconvolution (see below). The $^{20}\text{Ne}/^{22}\text{Ne}$ ratios range between 0.867 and 1.273, clearly indicating that Ne is dominantly cosmogenic with minor additional contributions. We determined cosmogenic ^{21}Ne concentrations and $^{22}\text{Ne}/^{21}\text{Ne}$ ratios (index cos) assuming that measured Ne is a mixture of cosmogenic Ne with $^{20}\text{Ne}/^{22}\text{Ne} = 0.867$, which is the lowest ratio measured for the samples, and atmospheric contamination ($^{20}\text{Ne}/^{22}\text{Ne} = 9.78$). The decomposed values are given in Table 1. The corrections for $^{21}\text{Ne}_{cos}$ are all negligible, <1%. The $(^{22}\text{Ne}/^{21}\text{Ne})_{cos}$ ratios range

between 1.025 and 1.098. As discussed earlier $(^{22}\text{Ne}/^{21}\text{Ne})_{cos}$ in the metal phase (hereafter labeled FeNi) range between 1.02 and 1.04 (cf. Ammon et al. 2008); ratios higher than this indicate contributions from phosphorous and/or sulfur. We recently measured $(^{22}\text{Ne}/^{21}\text{Ne})_{cos}$ of 1.21 ± 0.04 for two schreibersite inclusions from the large iron meteorite Twannberg (Smith et al. 2017). For our samples, most of the $(^{22}\text{Ne}/^{21}\text{Ne})_{cos}$ ratios indicate contributions from sulfur and/or phosphorous. We corrected the $^{21}\text{Ne}_{cos}$ concentrations for these contributions using the procedure developed by Ammon et al. (2008):

$$^{21}\text{Ne}_{\text{FeNi}} = {}^{21}\text{Ne}_{\text{corr}} = \frac{R_\text{M} - R_\text{S}}{R_{\text{FeNi}} - R_S} \times {}^{21}\text{Ne}_\text{m} \qquad (2)$$

where $^{21}\text{Ne}_\text{m}$ and R_M are the measured ^{21}Ne concentrations and $^{22}\text{Ne}/^{21}\text{Ne}$ ratios, respectively. The $(^{22}\text{Ne}/^{21}\text{Ne})_{cos}$ ratios for troilite/schreibersite inclusions and pure FeNi metal are R_s and R_{FeNi}, respectively. The $^{21}\text{Ne}_{\text{FeNi}}$ values corrected in this way are given in Table 1. The corrections are ~40% for Lombard and less than 1% for Bristol. On average, ~7% of the measured $^{21}\text{Ne}_{cos}$ is due to contributions from troilite and/or schreibersite, that is, the corrections are typically minor. The $^{21}\text{Ne}_{cos}$ production rates from *troilite* and *schreibersite* are on average 10 times higher than from pure metal (e.g., Ammon et al. 2008; Smith et al. 2017), which makes the ^{21}Ne production rates from sulfur and/or phosphorous 30–50 times higher than from iron and nickel. The measured $^{22}\text{Ne}/^{21}\text{Ne}$ ratios indicate sulfur and/or phosphorous concentrations in the range of 0.1–0.2 wt%, which is reasonable considering that we preselected the samples using only optical means. If we only consider the data for the IIIAB iron meteorites, the corrections for ^{21}Ne are ~6%. In contrast, the average correction for the iron meteorites from the other groups is slightly higher, that is, in the range of 10–12%. The $^{21}\text{Ne}_{\text{FeNi}}$ concentrations (in 10^{-8} cm^3 STP per g) range from 0.066 for Squaw Creek (IIAB) to 9.02 for Sandtown (IIIAB), that is, the variation among the studied samples is almost a factor of 137.

Argon

The $^{40}\text{Ar}/^{36}\text{Ar}$ and $^{36}\text{Ar}/^{38}\text{Ar}$ ratios and ^{38}Ar concentrations are given in Table A2 in Appendix A. The measured $^{40}\text{Ar}/^{36}\text{Ar}$ and $^{36}\text{Ar}/^{38}\text{Ar}$ ratios before blank correction range between 7–256 and 0.64–4.53, respectively, indicating that besides cosmogenic Ar, there is an additional component, most likely residual atmospheric contamination. We corrected the Ar data for the contamination assuming that all ^{40}Ar is atmospheric. The $^{36}\text{Ar}_{cos}$ and $^{38}\text{Ar}_{cos}$ concentrations are given in Table 1. The $(^{36}\text{Ar}/^{38}\text{Ar})_{cos}$ ratios range from

Table 1. Cosmogenic He, Ne, and Ar concentrations (in 10^{-8} cm^{3}STP per g) and isotopic compositions.

Sample	Group	^{3}He$_{cos}$	^{4}He$_{cos}$	^{21}Ne$_c$	$(^{22}$Ne/^{21}Ne$)_c$	^{21}Ne$_{corr}$	^{36}Ar$_c$	^{38}Ar$_c$
Avoca	IIIAB	635 ± 7	2273 ± 23	8.61 ± 0.35	1.034	8.18 ± 0.55	23.55 ± 0.92	37.25 ± 1.28
Arispe	IC	18.0 ± 0.2	72.7 ± 0.7	0.209 ± 0.009	1.081	0.146 ± 0.038	0.500 ± 0.020	0.803 ± 0.029
Benedict	IIIAB	602 ± 7	1167 ± 12	7.21 ± 0.30	1.036	6.77 ± 0.50	23.88 ± 0.96	38.64 ± 1.38
Boxhole	IIIAB	23.1 ± 0.2	96.8 ± 1.0	0.489 ± 0.020	1.053	0.414 ± 0.055	0.928 ± 0.037	1.623 ± 0.056
Braunau	IIAB	4.74 ± 0.05	18.8 ± 0.2	0.185 ± 0.009	1.027	0.182 ± 0.010	0.564 ± 0.022	0.883 ± 0.031
Bristol	IVA	n.d.	n.d.	5.26 ± 0.24	1.025	5.25 ± 0.24	13.32 ± 0.61	20.33 ± 0.85
Brownfield	IIB	n.d.	n.d.	4.53 ± 0.20	1.031	4.39 ± 0.27	11.18 ± 0.45	17.26 ± 0.60
Bur-Abor	IIIAB	438 ± 5	1603 ± 17	5.22 ± 0.21	1.036	4.92 ± 0.35	14.68 ± 0.58	23.66 ± 0.82
Calico Rock	IIA	n.d.	n.d.	5.16 ± 0.23	1.030	5.02 ± 0.29	17.09 ± 0.69	27.66 ± 0.95
Cape York	IIIAB	10.7 ± 0.1	69.4 ± 2.7	0.149 ± 0.06	1.028	0.146 ± 0.06	0.462 ± 0.019	0.717 ± 0.025
Carthage	IIIAB	124 ± 2	503 ± 6	1.28 ± 0.05	1.041	1.17 ± 0.10	0.003 ± 0.001	0.001 ± 0.001
Casas Grandes	IIIAB	55.3 ± 0.5	226 ± 2	0.435 ± 0.017	1.041	0.397 ± 0.035	1.531 ± 0.060	2.540 ± 0.088
Catalina 107	IIIAB	559 ± 6	1828 ± 18	6.67 ± 0.27	1.033	6.37 ± 0.41	15.72 ± 0.62	25.12 ± 0.87
Charcas	IIIAB	179 ± 2	675 ± 7	2.02 ± 0.08	1.043	1.82 ± 0.17	6.236 ± 0.244	10.06 ± 0.35
Chulafinnee	IIIAB	387 ± 4	1329 ± 18	4.66 ± 0.19	1.032	4.49 ± 0.27	13.20 ± 0.52	21.15 ± 0.73
Cincinnati	IIAB	277 ± 3	831 ± 9	4.05 ± 0.18	1.028	3.97 ± 0.22	11.16 ± 0.44	17.23 ± 0.59
Costilla Peak	IIIAB	533 ± 6	1604 ± 16	6.85 ± 0.27	1.030	6.67 ± 0.37	15.68 ± 3.86	24.01 ± 0.83
Dalton	IIIAB	274 ± 3	1027 ± 10	3.48 ± 0.14	1.036	3.28 ± 0.23	9.61 ± 0.38	15.52 ± 0.53
Davis Mountains	IIIAB	434 ± 5	1250 ± 13	4.70 ± 0.18	1.032	4.51 ± 0.27	13.55 ± 0.53	21.55 ± 0.74
Djebel-in-Azzene	IIIAB	634 ± 7	2016 ± 20	7.82 ± 0.32	1.027	7.72 ± 0.36	20.24 ± 0.80	31.94 ± 1.10
Durango	IIIAB	346 ± 4	1351 ± 14	4.20 ± 0.17	1.032	4.05 ± 0.24	11.76 ± 0.46	19.05 ± 0.66
Elyria	IIIAB	508 ± 5	1240 ± 12	6.48 ± 0.26	1.034	6.15 ± 0.41	21.45 ± 0.84	34.51 ± 1.22
Forsyth County	IIAB	46.1 ± 0.6	159 ± 2	0.624 ± 0.029	1.037	0.584 ± 0.047	1.850 ± 0.073	2.919 ± 0.101
Fort Pierre	IIIAB	n.d.	n.d.	6.83 ± 0.27	1.031	6.60 ± 0.38	16.89 ± 0.67	26.21 ± 0.91
Gan Gan	IVA	n.d.	n.d.	3.84 ± 0.17	1.035	3.63 ± 0.27	10.63 ± 0.42	16.98 ± 0.59
Gibeon	IVA	11.2 ± 0.1	72.2 ± 0.7	0.112 ± 0.005	1.033	0.107 ± 0.07	0.252 ± 0.010	0.320 ± 0.020
Grant	IIIAB	n.d.	n.d.	5.47 ± 0.13		3.46 ± 0.09	22.13 ± 1.40	33.36 ± 1.62
Greenbrier County	IIIAB	56.4 ± 0.6	110 ± 1	0.687 ± 0.028	1.032	0.662 ± 0.039	21.23 ± 0.84	34.02 ± 1.20
Henbury	IIIAB	133 ± 2	540 ± 5	1.87 ± 0.08	1.036	1.75 ± 0.13	4.602 ± 0.180	7.338 ± 0.253
Joel's Iron	IIIAB	47.1 ± 0.6	156 ± 2	0.685 ± 0.027	1.034	0.650 ± 0.043	20.84 ± 0.84	33.31 ± 1.20
Kayakent	IIIAB	56.9 ± 0.7	178 ± 2	0.800 ± 0.032	1.033	0.763 ± 0.049	2.419 ± 0.098	3.839 ± 0.138
Kenton County	IIIAB	476 ± 5	1738 ± 18	4.66 ± 0.19	1.035	4.41 ± 0.30	14.05 ± 0.55	22.37 ± 0.77
La Porte	IIIAB	214 ± 3	911 ± 10	2.27 ± 0.19	1.040	2.08 ± 0.18	6.511 ± 0.255	10.45 ± 0.36
Lombard	IIAB	13.8 ± 0.1	62.3 ± 0.6	0.172 ± 0.079	1.098	0.104 ± 0.039	0.419 ± 0.020	0.649 ± 0.027
Mapleton	IIIAB	n.d.	n.d.	3.14 ± 0.13	1.036	2.96 ± 0.21	11.41 ± 0.45	18.55 ± 0.64
Nazareth	IIIAB	556 ± 6	1539 ± 15	6.84 ± 0.28	1.027	6.76 ± 0.32	22.86 ± 0.93	36.92 ± 1.35
Norfolk	IIIAB	n.d.	n.d.	6.74 ± 0.27	1.033	6.45 ± 0.41	No relevant Ar	No relevant Ar
North Chile	IIAB	32.1 ± 0.3	207 ± 2	0.453 ± 0.021	1.050	0.392 ± 0.049	1.249 ± 0.049	2.034 ± 0.070
NWA 8442	IIIAB	72.6 ± 0.7	334 ± 3	1.04 ± 0.04	1.032	1.00 ± 0.06	2.760 ± 0.108	4.403 ± 0.152
Picacho	IIIAB	509 ± 5	1705 ± 17	5.83 ± 0.24	1.032	5.61 ± 0.34	21.09 ± 0.83	34.60 ± 1.21
Piñon	Ungr.	25.8 ± 0.3	102 ± 1	0.330 ± 0.015	1.062	0.265 ± 0.047	0.889 ± 0.038	1.420 ± 0.055
Plymouth	IIIAB	589 ± 9	1873 ± 23	8.02 ± 0.33	1.035	7.59 ± 0.53	20.10 ± 0.79	31.53 ± 1.09
Puente del Zacate	IIIAB	566 ± 6	1943 ± 20	7.06 ± 0.29	1.036	6.65 ± 0.48	19.80 ± 0.78	31.72 ± 1.09
Roebourne	IIIAB	202 ± 3	696 ± 8	2.40 ± 0.10	1.035	2.27 ± 0.16	6.023 ± 0.236	9.601 ± 0.331
Rowton	IIIAB	n.d.	n.d.	4.31 ± 0.17	1.034	4.09 ± 0.27	11.76 ± 0.46	18.59 ± 0.66
Sacramento Mountains	IIIAB	267 ± 4	902 ± 9	3.54 ± 0.14	1.029	3.45 ± 0.18	8.626 ± 0.338	13.50 ± 0.47
San Angelo	IIIAB	274 ± 3	1025 ± 11	2.81 ± 0.11	1.040	2.59 ± 0.22	9.005 ± 0.352	14.81 ± 0.51
Sandtown	IIIAB	620 ± 21	2070 ± 21	9.22 ± 0.37	1.029	9.02 ± 0.46	24.09 ± 0.94	37.51 ± 1.29
Schwetz	IIIAB	127 ± 1	207 ± 2	1.44 ± 0.06	1.041	1.32 ± 0.11	4.067 ± 0.162	6.67 ± 0.23
Sikhote-Alin	IIAB	230 ± 3	847 ± 9	2.39 ± 0.11	1.050	2.06 ± 0.26	6.592 ± 0.258	10.59 ± 0.37
Squaw Creek	IIAB	5.78 ± 0.06	22.9 ± 0.2	0.084 ± 0.004	1.064	0.066 ± 0.012	0.247 ± 0.011	0.395 ± 0.016
Tamentit	IIIAB	579 ± 6	1840 ± 19	6.90 ± 0.28	1.029	6.74 ± 0.36	18.47 ± 0.72	29.17 ± 1.00

Table 1. *Continued.* Cosmogenic He, Ne, and Ar concentrations (in 10^{-8} cm^{3}STP per g) and isotopic compositions.

Sample	Group	^{3}He$_{cos}$	^{4}He$_{cos}$	^{21}Ne$_c$	(^{22}Ne/ ^{21}Ne)$_c$	^{21}Ne$_{corr}$	^{36}Ar$_c$	^{38}Ar$_c$
Trenton	IIIAB	382 ± 5	1435 ± 16	4.22 ± 0.17	1.041	3.85 ± 0.34	0.001 ± 0.001	0.002 ± 0.001
Treysa	IIIAB	n.d.	n.d.	6.22 ± 0.25	1.031	6.01 ± 0.36	15.80 ± 0.63	25.01 ± 0.90
Turtle River	IIIAB	337 ± 4	1049 ± 11	4.77 ± 0.19	1.035	4.56 ± 0.32	12.59 ± 0.49	19.66 ± 0.68
Verkhne Udinsk	IIIAB	n.d.	n.d.	5.58 ± 0.22	1.034	5.32 ± 0.34	20.98 ± 0.88	32.1 ± 1.1
Zerhamra	IIIAB	124 ± 1	447 ± 5	1.89 ± 0.08	1.032	1.82 ± 0.11	5.49 ± 0.22	8.665 ± 0.299

The cosmogenic components are labeled "cos." The given uncertainties (1σ) include the uncertainties for (1) measurements of the ion currents, (2) corrections for interfering isotopes, (3) corrections for instrumental mass fractionation, and (4) corrections for trapped components, and (5) corrections for contributions from S and/or P on ^{21}Ne, that is, ^{21}Ne$_{corr}$. Systematic uncertainties in the calibration standard are not included; they amount to 4% for concentrations and 1% for isotope ratios.

0.57 ± 0.03 to 0.79 ± 0.06, indicating a clear cosmogenic signal (e.g., Wieler 2002). The samples from Trenton and Carthage were excluded because their $(^{36}$Ar/^{38}Ar)$_{cos}$ ratios after blank correction are 0.38 ± 0.03 and 2.70 ± 0.21, respectively, that is, far outside the cosmogenic range. Both meteorites have exceptionally low Ar concentrations, which make the measurements highly uncertain and which might explain the strange ratios. It is possible that both Ar fractions were accidentally lost during gas extraction. These data are not discussed any further.

The Isotopic Ratio (^{4}He/^{38}Ar)$_{cos}$

According to model predictions (Ammon et al. 2009), the (^{4}He/^{38}Ar)$_{cos}$ ratios are in the range of 35–115 for iron meteorites with pre-atmospheric radii between 10 and 120 cm. In contrast, the range of isotopic ratios found in this study varies from 3.2 for Greenbrier County to 226 for Gibeon, the range is much wider. The low ratio for Greenbrier County is most likely due to ^{4}He (and ^{3}He) deficits because not only is (^{4}He/^{38}Ar)$_{cos}$ much lower than the range given by the model predictions but also the (^{3}He/^{38}Ar)$_{cos}$ and (^{4}He/^{21}Ne)$_{cos}$ ratios are lower than the range defined by the other studied meteorites. Since the measured ^{3}He and ^{4}He concentrations for Greenbrier County are well within the range of concentrations measured for the other studied meteorites (Table A2 in Appendix A), we can exclude analytical problems and conclude that the ^{3}He and ^{4}He deficits occurred while the meteoroid traveled in space. Greenbrier County also exhibits a low (^{4}He/^{3}He) ratio of 1.95, further confirming that the He data are peculiar (see also above). The same argument holds for the iron meteorite Joel's Iron (^{4}He/^{38}Ar = 4.68), the measured ^{3}He and ^{4}He concentrations are not exceptionally low but the ratios (^{4}He/^{38}Ar)$_{cos}$, (^{3}He/^{38}Ar)$_{cos}$, and (^{4}He/^{21}Ne)$_{cos}$ are low. The (^{4}He/^{3}He) ratio for Joel's Iron is 3.31, which is within the range of the other meteorites, though at the lower end. The data

for Braunau are similar; all three isotopic ratios are low but in contrast to Greenbrier County and Joel's Iron, the ^{3}He and ^{4}He concentrations are also low. The perplexing nature of these observations leads us to reluctantly accept the possibility of unrecognized problems during the measurement. Additionally, the measured ^{4}He/^{3}He ratio is high, that is, 12.9, and we had to calculate ^{4}He$_{cos}$ = ^{3}He$_{cos}$ × 3.96 (see above). It might be possible that for Braunau, the value of 3.96 is too low, which then results in too low ^{4}He$_{cos}$ and consequently in too low ^{4}He/^{38}Ar and ^{4}He/^{21}Ne ratios. This, however, cannot explain the low (^{3}He/^{38}Ar)$_{cos}$ ratio. Anyway, ignoring the data for Greenbrier County, Joel's Iron, and Braunau reduces the measured range to 30–226, that is, the lower limit is in agreement with the model predictions. The lowest ratio is now for the iron meteorite Benedict, which has rather normal ^{3}He/^{38}Ar and ^{4}He/^{21}Ne ratios. The high ^{4}He/^{38}Ar ratio of ~226 for Gibeon is most likely due to the very low cosmogenic Ar concentration, which is either due to Ar loss during gas extraction and/or cleaning or it is due to the fact that the cosmogenic Ar concentration is extremely low due to the large pre-atmospheric size. Since the (^{21}Ne/^{38}Ar)$_{cos}$ ratio for Gibeon is slightly higher than the average for the other meteorites, we argue that the reason for the high (^{4}He/^{38}Ar)$_{cos}$ ratio is in a low ^{38}Ar concentration. Another explanation for high (^{4}He/^{38}Ar)$_{cos}$ ratios might be a complex exposure history. The depth dependency for production of ^{4}He$_{cos}$ and ^{38}Ar$_{cos}$ are different; ^{4}He$_{cos}$ is produced at greater depths than ^{38}Ar$_{cos}$. A sample that was originally buried deep in a large parent body might contain some ^{4}He$_{cos}$ but no ^{38}Ar$_{cos}$. After further breakup, there is production of ^{4}He$_{cos}$ and ^{38}Ar$_{cos}$, but the (^{4}He/^{38}Ar)$_{cos}$ ratio will always be too high due to the inherited ^{4}He$_{cos}$. Anyway, also excluding Gibeon from the data set reduces the measured (^{4}He/^{38}Ar)$_{cos}$ ratios to the range 30–101, that is, in agreement with the model predictions.

The Isotopic Ratio (^{4}He/^{21}Ne)$_{cos}$

The (^{4}He/^{21}Ne)$_{cos}$ ratios range between 157 for Schwetz and 675 for Gibeon. Using equation 16 from Honda et al. (2002), we can connect the (^{4}He/^{21}Ne)$_{cos}$ ratios to the pre-atmospheric shielding depth:

$$d = 7.34 \times 10^{-5} \times \left(\left(^4\text{He}/^{21}\text{Ne} \right)_{cos} \right)^{2.58} [\text{g cm}^{-2}] \quad (3)$$

Using corrected ^{21}Ne$_{cos}$ concentrations and considering only reliable ^{4}He$_{cos}$ concentrations, we calculate shielding depths in the range ~34 to ~1460 g cm^{-2}, which corresponds to depths—and accordingly—minima radii of 4.3 cm for Schwetz to 186 cm for Gibeon. The inferred minimum pre-atmospheric radius for Gibeon agrees with previous studies that inferred pre-atmospheric radii in the range 2–3 m (Bajo et al. 2008; Honda et al. 2008). The low (^{4}He/^{21}Ne)$_{cos}$ ratio for Schwetz and low minimal radius of 4.3 cm is in accord with the recovered mass of only 21.5 kg, which requires a pre-atmospheric radius of at least 8 cm. The large (^{4}He/^{21}Ne)$_{cos}$ ratio of 675 for Gibeon is expected due to its large pre-atmospheric size. The large iron meteorite Aletai (previously named Xinjiang, renamed in 2016), with a pre-atmospheric radius of more than 1 m, has an average (^{4}He/^{21}Ne)$_{cos}$ ratio of 593 ± 55 (Ammon et al. 2011). We measured (^{4}He/^{21}Ne)$_{cos}$ ratios in the range 295–756 for Twannberg, an extremely large iron meteorite; this ratio is slightly higher than that of Gibeon (Smith et al. 2017). In a systematic study of 12 different fragments from the large iron meteorite Canyon Diablo, Michlovich et al. (1994) measured (^{4}He/^{21}Ne)$_{cos}$ ratios that vary from ~280 to ~480. The average shielding depth, that is, the average minimum radius, for all meteorite samples studied by us is 284 g cm^{-2} or 36 cm. This average radius corresponds to an average mass of 1.5 t.

The Correlation (^{4}He/^{38}Ar)$_{cos}$ as a Function of (^{4}He/^{21}Ne)$_{cos}$

Figure 3 depicts the element ratios (^{4}He/^{38}Ar)$_{cos}$ as a function of (^{4}He/^{21}Ne)$_{cos}$ for the studied meteorites. There is a reasonable linear correlation with $R^2 = 0.98$. The slope of the correlation line, if forced through the origin, is 0.198 ± 0.005 (solid black line). The gray shaded area shows the 95% confidence interval. This finding confirms earlier results that the (^{4}He/^{38}Ar)$_{cos}$ ratios can together with or in addition to the (^{4}He/^{21}Ne)$_{cos}$ ratios also serve as a shielding indicator (e.g., Ammon et al. 2009). The (^{4}He/^{38}Ar)$_{cos}$ ratios can often be determined more reliably than (^{4}He/^{21}Ne)$_{cos}$ ratios because the latter are often compromised by contributions from sulfur and/or phosphorous to ^{21}Ne$_{cos}$. If such contributions are not properly

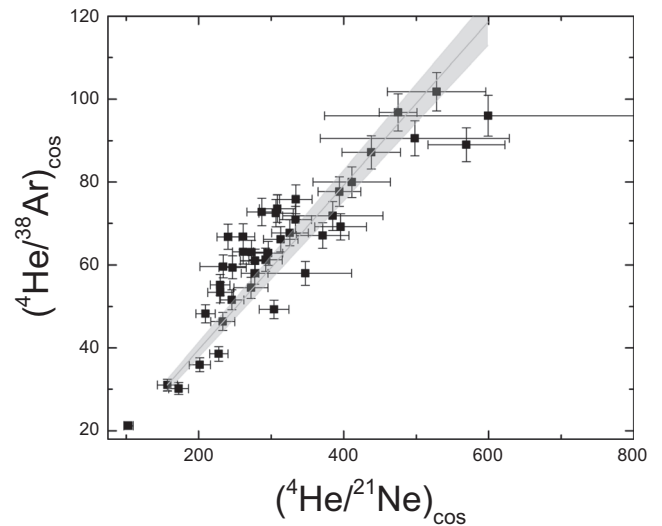Fig. 3. (^{4}He/^{38}Ar)$_{cos}$ as a function of (^{4}He/^{21}Ne)$_{cos}$ for the studied iron meteorites. There is a linear correlation between both elemental ratios, indicating that (^{4}He/^{38}Ar)$_{cos}$ can also be used as an indicator for shielding.

subtracted, the (^{4}He/^{21}Ne)$_{cos}$ ratios are too low, which results in an underestimation of the shielding conditions, that is, the size of the meteorite and shielding depth of the sample. Based on Equation 3 and by using the linear correlation between (^{4}He/^{38}Ar)$_{cos}$ and (^{4}He/^{21}Ne)$_{cos}$, we propose a new equation for calculating pre-atmospheric shielding depths for iron meteorites based on (^{4}He/^{38}Ar)$_{cos}$:

$$d = 4.78 \times 10^{-3} \times \left(\left(^4\text{He}/^{38}\text{Ar} \right)_{cos} \right)^{2.58} [\text{g cm}^{-2}] \quad (4)$$

Isotope Ratios ^{38}Ar/^{21}Ne

The ratios ^{38}Ar$_{cos}$/^{21}Ne$_{FeNi}$ for samples, except Trenton and Carthage, range between ~3 for Gibeon (IVA) and 51.3 for Joel's Iron (IIIAB), the grand average value is ~6.65. The ratio for Joel's Iron is much higher than the other ratios and must be considered as an outlier. The reason for this anomalously high ratio is most likely the low ^{21}Ne$_{FeNi}$ concentration, which is among the lowest in our database. In contrast, the ^{38}Ar$_{cos}$ concentration is well within the range defined by the other studied meteorites. If we exclude the ^{38}Ar$_{cos}$/^{21}Ne$_{FeNi}$ ratio for Joel's Iron from the database, the ratios range between ~3 and ~6.4 and the average value is ~4.8. For Twannberg, we measured slightly higher ^{38}Ar$_{cos}$/^{21}Ne$_{FeNi}$ ratios between ~2.8 and ~7.9 (Smith et al. 2017). Also, the average value of ~6.3 for Twannberg is slightly higher than the average value obtained here for a large selection of different iron meteorites.

Cosmogenic Radionuclides

The cosmogenic ^{10}Be, ^{26}Al, ^{36}Cl, and ^{41}Ca activities (dpm kg^{-1}) are given in Table A3 in Appendix A together with the Ni concentrations (%) measured via ICP-MS. The Fe concentrations [Fe] were calculated from the measured Ni concentrations [Ni] via [Fe] = 100–[Ni]. Some radionuclides in some samples, for example ^{10}Be, ^{26}Al, and ^{36}Cl in Gibeon, could not be quantified due to very low radionuclide concentrations, either due to high shielding depths, low chemical yield (Gibeon), handling losses, or other. The results are labeled "below detection limit (bdl)" in Table A3 in Appendix A. Among the measured radionuclides, ^{41}Ca is the most challenging to measure (Rugel et al. 2016). First, some samples have very low concentrations. Second, the chemical yields for some samples were low; for example, in the range of ~40% for Davis Mountains or Kenton County or even as low as ~15% for Henbury. All radionuclide data for Henbury are very close to the detection limit (see below). The major reason, however, for the substantially larger uncertainties of the ^{41}Ca concentrations of ~17% (average) compared to the other radionuclides is a significant isobar (^{41}K) contamination in the ion source, as described in Rugel et al. (2016) (from Cs used for sputtering or from migration from stainless steel pins used as backing), which compromised some of the measurements and/or interpretation of the results. Before we discuss the radionuclides in detail, we first need to correct the data for radioactive decay during terrestrial residence.

Terrestrial Ages

Most of the iron meteorites in this study are finds, so the radionuclide data for these meteorites must be corrected for decay during terrestrial residence (T_{terr}) before discussing production rates. We chose the ^{36}Cl and ^{41}Ca radionuclide pair because the commonly used ^{36}Cl/^{10}Be dating method is occasionally compromised by contributions from 0.1 to 0.2 wt% of P- and/or S-rich inclusions. In addition, ^{41}Ca has a shorter half-life compared to ^{10}Be (1.37×10^6 years for ^{10}Be versus 0.995×10^5 years for ^{41}Ca); it is more suitable for calculating terrestrial ages in the range typical for iron meteorites —from zero up to about 500 ka (Table 2, see also Smith et al. 2017). The basic equation is:

$$T_{terr} = \frac{1}{(\lambda_{36} - \lambda_{41})} \times \ln\left(\frac{\left(^{41}Ca/^{36}Cl\right)_{meas}}{P(^{41}Ca)/P(^{36}Cl)}\right) \quad (5)$$

where $\left(^{41}Ca/^{36}Cl\right)_{meas}$ is the measured ^{41}Ca/^{36}Cl ratio and λ_{36} and λ_{41} are the decay constants for ^{36}Cl and ^{41}Ca, respectively. For the ^{36}Cl decay constant, we use $\lambda_{36} = (2.301 \pm 0.011) \times 10^{-6}$ yr^{-1} (Nica et al. 2012). For the radioactive decay of ^{41}Ca, we use the new decay constant of $\lambda_{41} = (6.97 \pm 0.11) \times 10^{-6}$ yr^{-1} from Jörg et al. (2012), which is 4.7% higher than the earlier value of $\lambda_{41} = (6.66 \pm 0.32) \times 10^{-6}$ yr^{-1} by Kutschera et al. (1992). Using the new value of $\lambda_{41} = (6.97 \pm 0.11) \times 10^{-6}$ yr^{-1} is not without problems because most of the earlier data are based on the old value ($\lambda_{41} = [6.66 \pm 0.32] \times 10^{-6}$ yr^{-1}), which makes comparisons with earlier data difficult. To enable comparisons, all ^{41}Ca activities determined using the old half-life must be increased by 4.7%. In an earlier study, in which we used the old ^{41}Ca half-life, we used data for the meteorite falls Treysa, Sikhote-Alin, and Rowton together with data for two meteorites with known T_{terr}, that is, Grant and Morasko, to determine a ^{41}Ca/^{36}Cl production rate ratio of 1.105 ± 0.048 (Smith et al. 2017). From new model calculations (Smith et al. 2017), we were able to conclude that the ^{41}Ca/^{36}Cl production rate ratio is almost independent of shielding and can therefore be applied to all sizes of iron meteorites. Adjusting the earlier data to the new ^{41}Ca half-life gives an updated ^{41}Ca/^{36}Cl production rate ratio of 1.157 ± 0.050. Equation 5 becomes:

$$T_{terr} = \frac{1}{(\lambda_{36} - \lambda_{41})} \times \ln\left(\frac{\left(^{41}Ca/^{36}Cl\right)_{meas}}{(1.157 \pm 0.050)}\right) \quad (6)$$

The ^{41}Ca/^{36}Cl terrestrial ages are given in Table 2. The uncertainties are dominated by the uncertainties for the ^{41}Ca concentrations (17% on average) and by the uncertainty for the ^{41}Ca/^{36}Cl production rate ratio (~4.3%). Since the differences are well within typical uncertainties, the choice of the half-life has only a minor influence on T_{terr}, the CRE age, and on the CRE age histogram (see below). We cannot give T_{terr} for Arispe, Gan Gan, Gibeon, and Piñon due to missing ^{36}Cl and/or ^{41}Ca data. For Benedict, Brownfield, Catalina 107, and Mapleton, the measured ^{41}Ca/^{36}Cl ratios are slightly higher than the assumed production rate ratio of 1.157. However, there is still agreement within the (sometimes large) 1σ uncertainty. For these meteorites we assume $T_{terr} \equiv 0$. For the meteorites Boxhole, Fort Pierre, and Schwetz, the measured ^{41}Ca/^{36}Cl ratios are sometimes significantly higher than the assumed production rate ratio, though the discrepancy is still within the 2σ uncertainties. For the three meteorites, we also assume $T_{terr} \equiv 0$. For the four meteorites Braunau, Costilla Peak, Davis Mountains, and Zerhamra, the terrestrial ages are all <10 ka with uncertainties in the range 10–

Table 2. Terrestrial ages (^{36}Cl/^{41}Ca), ^{10}Be, ^{26}Al, and ^{36}Cl production rates (dpm kg^{-1}), and ^{36}Cl/^{36}Ar cosmic ray exposure (CRE) ages (Ma).

Sample	Group	Terrestrial age (ka)	^{10}Be(0)	^{26}Al(0)	^{36}Cl(0)	CRE age (Ma)
Avoca	IIIAB	45.4 ± 14.7	4.16 ± 0.12	2.91 ± 0.15	20.8 ± 0.8	482 ± 35
Arispe	IC	^{36}Cl not detected	—	—	—	—
Benedict	IIIAB	=0 (1σ)	5.02 ± 0.10	3.54 ± 0.25	24.4 ± 0.4	418 ± 27
Boxhole	IIIAB	=0 (2σ)	0.164 ± 0.04	0.13 ± 0.02	1.00 ± 0.08	395 ± 39
Braunau	IIAB	$9.8^{+13.4}_{-9.8}$	3.68 ± 0.07	2.76 ± 0.10	20.6 ± 0.7	11.7 ± 0.8
Bristol	IVA	503 ± 178	4.52 ± 1.14	3.29 ± 0.57	22.8 ± 9.4	250 ± 104
Brownfield	IIB	= 0 (1σ)	5.24 ± 0.10	3.60 ± 0.15	19.6 ± 0.7	243 ± 18
Bur-Abor	IIIAB	41.5 ± 12.8	3.40 ± 0.10	2.29 ± 0.13	17.0 ± 0.6	368 ± 26
Cape York	IIIAB	67.2 ± 406	0.090 ± 0.004	0.10 ± 0.04	0.503 ± 0.471	392 ± 367
Calico Rock	IIA	136 ± 35	5.96 ± 0.42	3.70 ± 0.20	19.7 ± 1.7	369 ± 39
Carthage	IIIAB	315 ± 33	1.81 ± 0.29	1.32 ± 0.13	10.7 ± 0.8	—
Casas Grandes	IIIAB	247 ± 98	0.633 ± 0.079	0.34 ± 0.06	1.50 ± 0.36	437 ± 109
Catalina 107	IIIAB	=0 (1σ)	4.51 ± 0.09	3.42 ± 0.19	21.4 ± 0.3	313 ± 20
Charcas	IIIAB	109 ± 18	1.54 ± 0.09	1.12 ± 0.11	9.38 ± 0.39	284 ± 21
Chulafinnee	IIIAB	25.3 ± 12.2	4.70 ± 0.11	3.26 ± 0.17	23.1 ± 0.7	244 ± 17
Cincinnati	IIAB	61.8 ± 13.6	5.69 ± 0.21	4.06 ± 0.15	23.6 ± 0.8	202 ± 14
Costilla Peak	IIIAB	1.22 ± 11.6	5.37 ± 0.11	3.59 ± 0.13	22.0 ± 0.7	304 ± 77
Dalton	IIIAB	40.6 ± 13.3	3.37 ± 0.09	2.32 ± 0.16	18.1 ± 0.6	227 ± 16
Davis Mountains	IIIAB	2.9 ± 12.8	2.69 ± 0.05	1.85 ± 0.09	13.9 ± 0.5	415 ± 29
Djebel-in-Azzene	IIIAB	192 ± 22	5.79 ± 0.57	4.65 ± 0.20	20.3 ± 1.1	425 ± 35
Durango	IIIAB	153 ± 19	1.83 ± 0.14	1.40 ± 0.09	14.3 ± 0.6	352 ± 27
Elyria	IIIAB	19.7 ± 12.8	5.10 ± 0.11	3.50 ± 0.19	25.3 ± 0.8	362 ± 25
Forsyth County	IIAB	187 ± 19	4.17 ± 0.40	2.99 ± 0.20	18.5 ± 0.8	43 ± 3
Fort Pierre	IIIAB	= 0 (2σ)	5.23 ± 0.10	3.51 ± 0.13	21.6 ± 0.3	333 ± 21
Gan Gan	IVA	^{36}Cl not detected	—	—	—	—
Gibeon	IVA	^{36}Cl & ^{41}Ca not detected	—	—	—	—
Grant	IIIAB	13.2 ± 14.9	Sample lost	1.59 ± 0.40	14.7 ± 0.5	642 ± 56
Greenbrier County	IIIAB	62.2 ± 12.7	4.16 ± 0.15	2.97 ± 0.14	29.3 ± 0.9	309 ± 22
Henbury	IIIAB	148 ± 33[a]	Too low	Too low	Too low	—
Joel's Iron	IIIAB	26.6 ± 30.2	4.65 ± 0.11	3.07 ± 0.20	20.3 ± 1.4	438 ± 41
Kayakent	IIIAB	=0 (fall)	4.32 ± 0.09	2.69 ± 0.14	19.8 ± 0.4	52 ± 3
Kenton County	IIIAB	554 ± 60	2.41 ± 0.67	1.42 ± 0.13	9.19 ± 1.28	652 ± 99
La Porte	IIIAB	28.9 ± 12.5	4.70 ± 0.12	3.02 ± 0.21	20.4 ± 0.7	136 ± 10
Lombard	IIAB	5.31 ± 36.1	0.543 ± 0.011	0.26 ± 0.11	3.15 ± 0.27	57 ± 6
Mapleton	IIIAB	=0 (1σ)	3.92 ± 0.07	2.66 ± 0.14	19.5 ± 0.25	250 ± 16
Nazareth	IIIAB	2.25 ± 13.1	1.47 ± 0.06	3.39 ± 0.16	22.8 ± 0.7	428 ± 30
Norfolk	IIIAB	6.3 ± 40.7	5.18 ± 0.10	3.35 ± 0.23	20.9 ± 2.0	—
North Chile	IIAB	562 ± 86.1	1.40 ± 0.40	0.84 ± 0.15	6.09 ± 1.21	87 ± 18
NWA 8442	IIIAB	39.2 ± 15.2	2.47 ± 0.07	1.58 ± 0.08	13.0 ± 0.5	90 ± 7
Picacho	IIIAB	96.5 ± 16.3	4.12 ± 0.09	2.78 ± 0.21	20.8 ± 0.8	433 ± 32
Piñon	Ungr.	^{36}Cl not detected	—	—	—	—
Plymouth	IIIAB	19.8 ± 12.0	4.88 ± 0.10	3.07 ± 0.23	23.8 ± 0.7	361 ± 25
Puente del Zacate	IIIAB	285 ± 28	3.60 ± 0.52	2.23 ± 0.18	13.8 ± 0.9	614 ± 55
Roebourne	IIIAB	33.5 ± 12.7	4.46 ± 0.11	3.33 ± 0.21	21.7 ± 0.7	118 ± 8
Rowton	IIIAB	11.6 ± 22.0	5.03 ± 0.11	3.31 ± 0.20	21.8 ± 1.2	230 ± 19
Sacramento Mountains	IIIAB	148 ± 17	3.90 ± 0.30	2.51 ± 0.12	18.2 ± 0.7	202 ± 15
San Angelo	IIIAB	105 ± 21	1.60 ± 0.09	1.05 ± 0.09	8.72 ± 0.44	440 ± 35
Sandtown	IIIAB	26.3 ± 13.0	5.01 ± 0.12	3.41 ± 0.12	22.1 ± 0.7	465 ± 33
Schwetz	IIIAB	= 0 (2σ)	1.41 ± 0.03	0.94 ± 0.09	7.01 ± 0.15	247 ± 16
Sikhote-Alin	IIAB	=0 (fall)	1.37 ± 0.03	0.88 ± 0.10	7.30 ± 0.09	385 ± 24
Squaw Creek	IIAB	69.6 ± 21.4	4.79 ± 0.19	2.76 ± 0.44	24.4 ± 1.3	4.3 ± 0.4
Tamentit	IIIAB	17.3 ± 16.1	4.25 ± 0.09	2.91 ± 0.14	19.2 ± 0.8	410 ± 30
Trenton	IIIAB	$2.7^{+13.8}_{-2.7}$	2.56 ± 0.05	1.66 ± 0.13	13.5 ± 0.5	—

Table 2. *Continued.* Terrestrial ages ($^{36}Cl/^{41}Ca$), ^{10}Be, ^{26}Al, and ^{36}Cl production rates (dpm kg^{-1}), and $^{36}Cl/^{36}Ar$ cosmic ray exposure (CRE) ages (Ma).

Sample	Group	Terrestrial age (ka)	$^{10}Be(0)$	$^{26}Al(0)$	$^{36}Cl(0)$	CRE age (Ma)
Treysa	IIIAB	=0 (fall)	4.69 ± 0.10	3.24 ± 0.15	20.3 ± 0.3	332 ± 21
Turtle River	IIIAB	32.2 ± 13.6	5.38 ± 0.12	3.62 ± 0.22	23.9 ± 0.9	225 ± 16
Verkhne Udinsk	IIIAB	=0 (set)	2.69 ± 0.05	1.11 ± 0.06	22.8 ± 0.5	393 ± 26
Zerhamra	IIIAB	7.3 ± 15.2	3.80 ± 0.08	2.79 ± 0.16	18.9 ± 0.7	124 ± 9

The uncertainties for the ^{26}Al and ^{36}Cl production rates, that is, $^{26}Al(0)$ and $^{36}Cl(0)$, are calculated using Gaussian error propagation and considering the uncertainties for the radionuclide activities (Table A2 in Appendix A) and the uncertainties for the terrestrial ages but not the uncertainties for the decay constants. For $^{26}Al(0)$, we also consider uncertainties introduced by the correction for contributions from S and/or P (see text).
[a]Data are from Shankar et al. (2011)

15 ka. A similar problem exists for the three meteorites Joel's Iron, Lombard, and Rowton, though the uncertainties for the ages are significantly higher, in the range 22–36 ka, due to higher uncertainties for the measured ^{41}Ca concentrations. The data for Cape York are unreliable, the uncertainty of the age is significantly higher than the age, which is due to exceptionally high uncertainties of the ^{41}Ca concentrations, which are very close to the detection limit. For Henbury, the measured $^{41}Ca/^{36}Cl$ ratio is unreasonably high (i.e., 4.1 ± 2.4) due to a very low ^{36}Cl concentration of only 0.068 dpm kg^{-1}, which is by far the lowest value quantified in our study besides the already mentioned Gibeon. Since we cannot give T_{terr} for Henbury, we use the $T_{terr} = 148 ± 33$ ka determined by Shankar et al. (2011) using the $^{36}Cl/^{10}Be$ method (see also Lavielle et al. 1999). The very high T_{terr} for Verkhne Udinsk of more than 1.2 Ma is suspect considering the rather normal ^{36}Cl concentration of 22.76 ± 0.50 dpm kg^{-1}, which is close to the saturation value. We consider the ^{41}Ca concentrations too low but errors, during chemical extraction or AMS measurements cannot be an explanation. Since the ^{36}Cl concentration is rather normal, we assume $T_{terr} \equiv 0$.

The 53 terrestrial ages obtained by us are in good agreement with literature data that are usually obtained using the less reliable $^{36}Cl/^{10}Be$ method. The terrestrial age for Grant of $13.2^{+14.9}_{-13.2}$ ka is in agreement with ages obtained by Lavielle et al. (1999) and Shankar (2011) of 22 ± 20 ka and 43 ± 49 ka, respectively, that is, all three studies indicate a short T_{terr}. The T_{terr} for Norfolk of essentially zero is in agreement with the very short $T_{terr} = 35±20$ ka determined by Lavielle et al. (1999). For Picacho, we determined $T_{terr} = 96.5 ± 16.3$ ka, which is in agreement with the ages of 76 ± 29 ka and 129 ± 44 ka determined by Shankar (2011) and Lavielle et al. (1999), respectively. The age obtained by us for Sacramento Mountains of 148 ± 17 ka is in perfect agreement with the age of 148 ± 25 ka given by Shankar (2011).

The terrestrial ages range from essentially zero for Benedict, Boxhole, Brownfield, Catalina 107, Fort Pierre, Kayakent, Mapleton, and Schwetz to 562 ± 86 ka for North Chile. Twelve meteorites out of the 53 for which we have data have T_{terr} larger than 100 ka, long for T_{terr} in nonpolar regions. Long T_{terr} for some large iron meteorites were also reported by Aylmer et al. (1988) and Chang and Wänke (1969). For example, using the $^{10}Be/^{36}Cl$ radionuclide pair, Chang and Wänke (1969) determined for the iron meteorite Tamarugal (Chile) a terrestrial age of ~2.7 Ma. In addition, long terrestrial ages were also observed by Nishiizumi et al. (2002) for a Martian and a lunar meteorite from a hot desert region.

We recently published a long terrestrial age of 202 ± 34 ka for the large IIG iron meteorite Twannberg (Smith et al. 2017). By restudying the age using not only the new ^{41}Ca half-life but also applying an isochron technique based on the five measured Twannberg samples, we calculated a new $^{41}Ca/^{36}Cl$ ratio of 0.508 ± 0.050, which corresponds to an age of 176 ± 19 ka, slightly lower than our former result. While this long T_{terr} is still surprising considering the humid conditions in Switzerland, it is well within the range of T_{terr} values determined here. For example, T_{terr} for Twannberg is very similar to T_{terr} of Forsyth County (187 ± 19 ka) and Djebel-in-Azzene (192 ± 22 ka). While Djebel-in-Azzene was found in Algeria and experienced more arid conditions, Forsyth County, Kenton County, and Bristol, which all have T_{terr} similar to or even longer than Twannberg, were found in the east of the USA, that is, also in humid conditions.

Combining all data, we conclude that T_{terr} for iron meteorites can be as long as a few hundred ka, even in humid environmental conditions. As we already speculated for the discussion of the Twannberg data, there might be a process responsible for avoiding or slowing down weathering processes in iron meteorites.

Production Rates and Production Rate Ratios

Here, we discuss the ^{10}Be, ^{26}Al, and ^{36}Cl production rates, that is, the concentrations at time of fall. With

the known terrestrial ages, it is straightforward calculating production rates for ^{36}Cl. For ^{10}Be and ^{26}Al, the situation is more complicated because both radionuclides can be compromised by contributions from S and/or P. Consequently, ^{10}Be and ^{26}Al production rates not only depend on shielding but also on the trace element concentrations of the studied sample. The correction procedure as well as how we treated the uncertainties is described in detail in Appendix B.

The corrections for ^{26}Al are <10%; exceptions are Charcas (correction factor 1.10), Sikhote-Alin (1.16), Boxhole (1.18), Piñon (1.25), Squaw Creek (1.27), Arispe (1.43), and Lombard (1.66). The corrections for ^{10}Be are smaller than the corrections for ^{26}Al. The ^{10}Be, ^{26}Al (corrected), and ^{36}Cl concentrations at the time of fall, that is, the production rates, are given in Table 2. Production rates for ^{41}Ca are not given because they are no longer independent; ^{41}Ca production rates are simply given by 1.157 times the ^{36}Cl production rates.

The ^{10}Be, ^{26}Al, and ^{36}Cl production rates for Cape York, Casas Grandes, Henbury, and Lombard are all low, indicating a large pre-atmospheric size. For Lombard and Casas Grandes, this finding is in accord with high ^{4}He/^{21}Ne ratios of 600 and 569, respectively. In contrast, the ^{4}He/^{21}Ne ratios of 309 for Henbury and 290 for Cape York are not exceptionally high and are therefore in contradiction to the low radionuclide production rates. The low ^{4}He/^{21}Ne ratio for Cape York is surprising because with a recovered mass of more than 58 t Cape York was obviously a large object. Since the CRE age for Henbury is unreasonably high due to the low ^{36}Cl concentration (see below), we consider all radionuclide production rates for Henbury as unreliable; they are not considered any further.

The ^{10}Be production rates range between 0.09 dpm kg^{-1} for Gibeon and 5.96 dpm kg^{-1} for Calico Rock; the average is 3.60 dpm kg^{-1}. The data are well within the range typical for iron meteorites. For example, Aylmer et al. (1988), Lavielle et al. (1999), and Xue et al. (1995) determined ^{10}Be production rates in the range 3–6 dpm kg^{-1}. In a recent study, Shankar et al. (2011) measured ^{10}Be production rates in the range 0.36–6.00 dpm kg^{-1}. Figure 4 depicts the ^{10}Be production rates as a function of (^{4}He/^{21}Ne)$_{cos}$. As expected, the ^{10}Be production rates decrease with increasing (^{4}He/^{21}Ne)$_{cos}$ ratios, that is, with increasing shielding. Also shown is the correlation line given by Aylmer et al. (1988), which is only slightly different from the correlation line given earlier by Chang and Wänke (1969). Our data are in accord with the correlation line, despite the fact that the data by Aylmer et al. (1988) and Chang and Wänke (1969) are, first, based on different ^{10}Be half-lives and, second, their
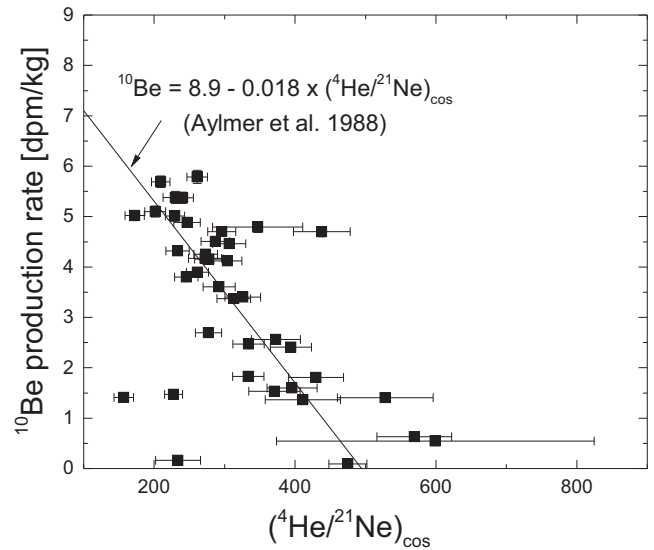

Fig. 4. ^{10}Be production rate as a function of (^{4}He/^{21}Ne)$_{cos}$. Also shown is the linear correlation line given by Aylmer et al. (1988).

^{21}Ne data are not corrected for contributions from S and/or P. While this all indicates consistency, this correlation is not useful. The substantial scatter precludes the determination of the shielding conditions only via ^{10}Be.

The (corrected) ^{26}Al production rates measured here range from 0.10 dpm kg^{-1} for Cape York to 4.65 dpm kg^{-1} for Djebel-in-Azzene; the average value is 2.46 dpm kg^{-1}. Again, the results are in agreement with literature values that are usually in the range 2–5 dpm kg^{-1} (e.g., Aylmer et al. 1988; Xue et al. 1995; Lavielle et al. 1999). In a recent study, Shankar et al. (2011) determined ^{26}Al production rates between 0.27 and 5.07 dpm kg^{-1}.

To check the data for reliability, we calculated the ^{10}Be/^{26}Al production rate ratio. Published ratios are 1.3 ± 0.1 (Xue et al. 1995) and 1.4 ± 0.2 (Lavielle et al. 1999). The average for our data is 1.48 ± 0.26, that is, in agreement with literature data. There are, however, outliers that have ^{10}Be/^{26}Al production rate ratios that differ from the average by more than the standard deviation. The ratio for Nazareth of ~0.44 is too low. In contrast, the ratio for Verkhne Udinsk is too high compared to the average value; the difference is ~3 times the standard deviation. By not considering the outliers, we calculated a weighted average value of 1.45 ± 0.02 (using the uncertainties as weights). Here we want to stress that our average value is based on 49 individual data, which makes our value most likely more accurate than the earlier literature data.

The ^{36}Cl production rates range between 0.5 dpm kg^{-1} for Cape York and 29.3 dpm kg^{-1} for

Greenbrier County. The low value for Cape York is in accord with the ^{10}Be and ^{26}Al production rates, which are also low for this meteorite. The value of 29.3 $\pm$ 0.9 dpm kg^{-1} for Greenbrier County is unexpectedly high. According to our improved model calculations (Smith et al. 2017), the upper limit for the ^{36}Cl production rate is ~25 dpm kg^{-1}, which is well in accord with our data. For example, the second highest ^{36}Cl production rate is 25.3 $\pm$ 0.8 for Elyria. Currently, however, we have no reason to consider the data for Greenbrier County as unreliable and we might speculate that some of the excess ^{36}Cl has been produced in Cl-bearing inclusions.

CRE Ages

We calculated the CRE ages using the ^{36}Cl-^{36}Ar dating system, which is very reliable because almost 90% of the cosmogenic ^{36}Ar is from the isobaric decay of ^{36}Cl. Consequently, the ^{36}Cl production rate is an excellent proxy for the ^{36}Ar production rate, which makes the system very reliable and almost independent on shielding conditions and chemical composition, provided the cosmic ray flux is constant. Using this system, the CRE age is given by (e.g., Begemann et al. 1976; Lavielle et al. 1999):

$$T_{36-36} = \frac{1}{\lambda_{36}} \times \frac{P(^{36}Cl)}{P(^{36}Ar)} \times \frac{^{36}Ar}{^{36}Cl}$$
$$= 511 \times (0.835 \pm 0.040) \times \frac{^{36}Ar_{cos}}{^{36}Cl_0} [Ma] \quad (7)$$

where $P(^{36}Cl)/P(^{36}Ar)$ is the production rate ratio. The cosmogenic nuclide concentrations are $^{36}Ar_{cos}$ (10^{-8} cm^3 STP g^{-1}) and $^{36}Cl_{(0)}$ (dpm kg^{-1}), and λ_{36} (2.301×10^{-6} yr^{-1}; Nica et al. 2012) is the ^{36}Cl decay constant. The factor 511 corrects for the different units and includes the decay constant. For the production rate ratio, we use the value of 0.835 $\pm$ 0.040 from Lavielle et al. (1999).

The CRE ages range between ~4 Ma for Squaw Creek and ~640 Ma for Grant (Table 2). Our results agree well with the available literature data. For example, Lavielle et al. (1999) and Shankar (2011) determined for Brownfield CRE ages of 207 $\pm$ 6 and 194 $\pm$ 33 Ma, in agreement within two sigma with our result of 243 $\pm$ 18 Ma. Published CRE ages for Grant range from 426 $\pm$ 9 Ma to 640 $\pm$ 100 Ma (cf. Lipschutz et al. 1965; Lavielle et al. 1999; Ammon et al. 2008; Shankar et al. 2011; Schaeffer and Heymann 1965). Here, we determined a CRE age of 642 $\pm$ 39 Ma. The published CRE ages for Picacho of 453 $\pm$ 32 Ma (Lavielle et al. 1999) and 430 $\pm$ 13 Ma

(Shankar 2011) agree well with our age of 433 $\pm$ 27 Ma. For Sacramento Mountains, we determined a CRE age of 202 $\pm$ 13 Ma, that is, in agreement with the 209 $\pm$ 14 Ma given by Lavielle et al. (1999). Also, our CRE age of 385 $\pm$ 24 Ma for Sikhote-Alin is in agreement with an earlier result of 320 $\pm$ 150 Ma (Lipschutz et al. 1965).

There are, however, also some discrepancies. The CRE age for Lombard of 57 $\pm$ 6 Ma is significantly lower than the value of 301 $\pm$ 18 Ma given by Lavielle et al. (1999). The reason for this discrepancy is in the ^{36}Ar$_{cos}$ concentrations. While we measured a low ^{36}Ar$_{cos}$ concentration of only ~0.4 $\times$ 10^{-8} cm^{3}STP g^{-1}, Lavielle et al. (1999) measured a ^{36}Ar$_{cos}$ concentration of ~2.4 $\times$ 10^{-8} cm^{3}STP g^{-1}; that is, about six times higher. In contrast, the ^{36}Cl production rates are almost identical, 3.2 $\pm$ 0.2 dpm kg^{-1} in our study and 3.43 $\times$ 0.20 dpm kg^{-1} for Lavielle et al. (1999). Despite the finding that the noble gas ratios ^{3}He/^{38}Ar and ^{21}Ne/^{38}Ar measured by us for Lombard fit well into the range given by the other meteorites, we consider our data as unreliable. From our data, we determined ^{26}Al/^{21}Ne and ^{10}Be/^{21}Ne production rate ratios (atom/atom) of 1.5 $\pm$ 0.8 and 3.1 $\pm$ 1.2, which are unreasonably high compared to expected values of 0.35 and 0.55 (e.g., Lavielle et al. 1999) and therefore also indicate a too low CRE age. For further discussion, we use for Lombard the CRE age given by Lavielle et al. (1999). For Treysa, we calculate a CRE age of 332 $\pm$ 21 Ma, significantly different from the age of 530 Ma given by Lipschutz et al. (1965). However, these authors used the ^{21}Ne-^{26}Al dating system, which we consider as unreliable due to interfering contributions from S and/or P. The CRE ages of 430 $\pm$ 40 Ma and 370 $\pm$ 30 Ma, based, respectively, on the ^{36}Cl-^{36}Ar and ^{39}Ar-^{38}Ar pairs, given by Schaeffer and Heymann (1965) agree slightly better with our result. Note that Schaeffer and Heymann (1965) used the differences between the ^{36}Cl-^{36}Ar and ^{39}Ar-^{38}Ar CRE ages for Treysa to discuss cosmic ray intensity variations.

We use the production rate ratios ^{26}Al/^{21}Ne and ^{10}Be/^{21}Ne as a proxy for the reliability of the CRE ages. The ^{21}Ne production rates were calculated by dividing the corrected ^{21}Ne concentrations by the CRE ages. Therefore, incorrect CRE ages would lead to incorrect ^{21}Ne production rates. By considering all data, we calculated a weighted average ^{26}Al/^{21}Ne ratio of 0.35, that is, in agreement with the value of 0.38 given by Hampel and Schaeffer (1979). There are, however, some outliers. The ^{26}Al/^{21}Ne production rate ratio of 2.71 $\pm$ 0.26 for Greenbrier County is too high. The reason is most likely in the too low ^{21}Ne$_{FeNi}$ concentrations as it is indicated by a low $(^{21}$Ne/^{38}Ar$)_{cos}$

ratio of 0.02 as opposed to typical ratios of 0.2 for most of the other iron meteorites. We assume that the problem is in the $^{21}Ne_{FeNi}$ concentration and not in the $^{36}Ar_{cos}$ concentration and consider the CRE age for Greenbrier County as reliable. The same argument holds for Joel's Iron. The measured $(^{21}Ne/^{38}Ar)_{cos}$ ratio is about 10 times lower than the average, making the $^{21}Ne_{FeNi}$ data questionable. Again, we consider the CRE age as reliable. Finally, the $^{26}Al/^{21}Ne$ production rate ratio for Verkhne Udinsk of 0.16 ± 0.02 is too low. However, the $(^{21}Ne/^{38}Ar)_{cos}$ ratio of 0.16 is reasonable. Remember that the terrestrial age for Verkhne Udinsk was set to zero (see above). If this assumption is not true, this would explain the low ratio. However, a nonzero terrestrial age would increase the ^{36}Cl production rate and therefore reduce the CRE age, which in turn would reduce the $^{26}Al/^{21}Ne$ production rate ratio even more. Consequently, there is no coherent explanation for the low $^{26}Al/^{21}Ne$ production rate ratio for Verkhne Udinsk. Considering only the reliable data, for example, excluding Greenbrier County, Joel's Iron, and Lombard (see above), we calculate a weighted $^{26}Al/^{21}Ne$ production rate ratio of 0.32 ± 0.01 ($n = 46$), that is, slightly lower than the value used before. Using the same procedure for the $^{10}Be/^{21}Ne$ production rate ratio we calculate 0.44 ± 0.03 ($n = 48$), that is, lower than the value of 0.55 as used before (e.g., Lavielle et al. 1999). There is no dependency of the production rate ratios $^{10}Be/^{21}Ne$ and $^{26}Al/^{21}Ne$ on the $(^{4}He/^{21}Ne)_{cos}$ ratios, that is, on the shielding conditions.

THE CRE AGE HISTOGRAM

Figure 5 depicts the CRE age histogram for iron meteorites. In addition to the data from Table 2, we also included the CRE age for Twannberg of 193 ± 43 Ma, which differs slightly from the CRE age given by Smith et al. (2017). This change is due to a new terrestrial age (176 ka instead of 202 ka, see above) that changed the ^{36}Cl production rate and consequently the CRE age. In total, we determined CRE ages for 48 iron meteorites. In addition, we also considered the data from Lavielle et al. (1999) for Ainsworth, Bendego, Bohumilitz, Carlton, Huizopa, Lombard, Merceditas, Morradal, Nelson County, Norfolk, Surprise Springs, Yanhuitlan, and Yardymly ($n = 13$). For Brownfield, Grant, and Picacho, we used our data. For the discussion of the Lombard data, see above. From the study by Shankar et al. (2011), we used the CRE ages for Cape of Good Hope, Charlotte, Gibeon, Henbury, Hoba, and Tlacotepec ($n = 6$). We decided to also use the data from the two other studies because they are consistent with ours and it is therefore not expected that any bias is introduced.
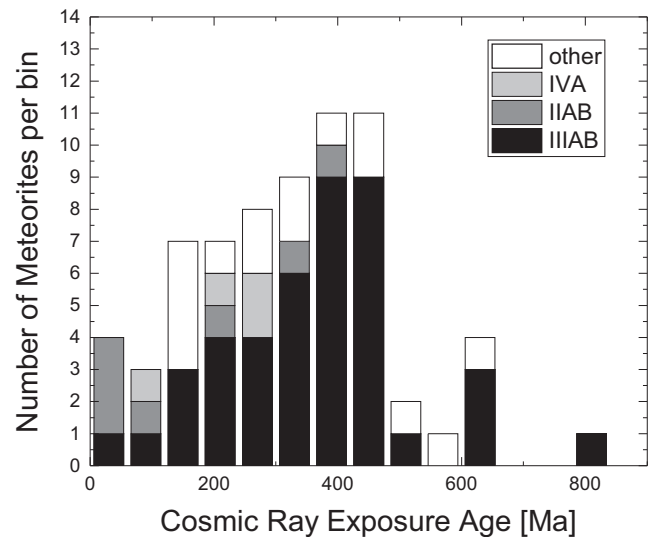

Fig. 5. Cosmic ray exposure age histogram for 68 iron meteorites. In addition to the 48 data from this study, we also show data from the study by Lavielle et al. (1999) and Shankar et al. (2011). The data are not corrected for pairing.

In total, the CRE age histogram consists of 68 iron meteorites (including Twannberg).

We have chosen a bin size of 60 Ma, which corresponds to about twice the average uncertainty of the CRE ages. The argument for the relatively wide bin size is as follows. First, with a normal distribution of the individual uncertainties of the CRE ages, the probability of assigning an age into a wrong bin is more than 60% if the bin size corresponds to 1σ but is only 40–50% if the bin size is 2σ. Second, a range of CRE ages from essentially zero up to 827 Ma and a bin size of 60 Ma results in 14 bins. With 68 iron meteorites in total, we have 4.9 meteorites per bin for a uniform distribution. Although this is still a low number, it might be sufficient to detect time-dependent structures.

At first glance, the CRE age histogram indicates that the delivery of iron meteorites to the Earth is not continuous but that most of the (studied) iron meteorites were produced in just a few major collisions. Based on the data shown in Fig. 5, one could argue for at least two peaks, one at 400 and at 630 Ma. For example, the 13 IIIAB iron meteorites Benedict, Boxhole, Cape York, Casas Grandes, Davis Mountains, Djebel-in-Azzene, Joel's Iron, Nazareth, Picacho, San Angelo, Tamentit, Verkhne Udinsk, and Merceditas have CRE ages that agree within their uncertainties. It is therefore possible that all 13 meteorites were ejected in one single large impact event on the IIIAB parent body, that is, that they are all launch paired. Typically one distinguishes launch pairing and fall pairing. Meteorites that are launch paired have been ejected

from the same parent body and have been produced in the same ejection event. The fall on the Earth, however, could have been at different times; only the sum of the CRE age and the terrestrial age, typically called ejection age, is the same for launch paired objects. In contrast, fall paired meteorites originate from the same pre-atmospheric meteoroid that broke up into smaller fragments during atmospheric entry. These fragments have the same CRE age and the same terrestrial age. Since the terrestrial ages for iron meteorites are usually much shorter than the CRE ages, we consider meteorites launch paired if they come from the same parent body, that is, the same chemical group, and if their CRE ages are identical to within 30 Ma or within the individual uncertainties (whatever is larger). With this assumption, we consider the following iron meteorites as paired (group, weighted average of CRE ages):

1 Avoca, Sandtown, Norfolk (IIIAB, 463 ± 17 Ma).
2 Benedict, Boxhole, Cape York, Casas Grandes, Davis Mountains, Djebel-in-Azzene, Joel's Iron, Nazareth, Picacho, San Angelo, Tamentit, Verkhne Udinsk, Merceditas (IIIAB, 425 ± 7 Ma).
3 Bur-Abor, Durango, Elyria, Plymouth (IIIAB, 361 ± 13 Ma).
4 Catalina 107, Costilla Peak, Fort Pierre, Greenbrier County (IIIAB, 318 ± 12 Ma).
5 Chulafinnee, Dalton, Mapleton, Rowton, Schwetz (IIIAB, 240 ± 7 Ma).
6 Grant, Kenton County, Puente del Zacate (IIIAB, 631 ± 36).
7 Roebourne and Zerhamra (IIIAB, 121 ± 6 Ma).
8 Huizopa and Bristol (IVA, 247 ± 32 Ma).

Using the individual uncertainties as weights for calculating averages is not without problems because some of the uncertainties are correlated (through the uncertainties of the production rates). However, since these uncertainties influence all data in the same way, they give similar weights and therefore do not compromise the calculated average. The CRE age histogram after correction for pairing is shown in Fig. 6. After considering pairing, there are 15 individual ejection events for IIIAB meteorites, seven individual events for IIAB iron meteorites, four individual events for IVA iron meteorites, and 15 individual ejection events for all the other studied iron meteorites. At first glance, there are still some indications for peaks in the CRE age histogram. However, the small number of events precludes statistically significant assessments; most of the peaks are not statistically significant, especially not if one considers each of the four groups separately. There is, however, an interesting result: the large number of iron meteorites ($n = 13$) that are likely ejected from only one impact event at ~425 Ma (second
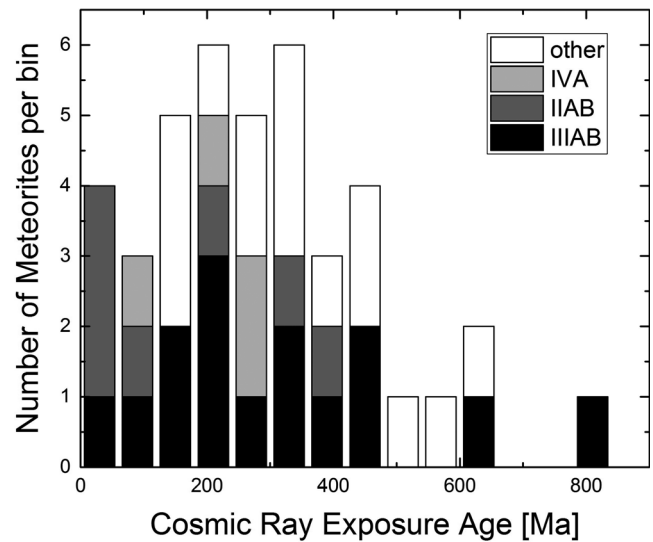

Fig. 6. Cosmic ray exposure age histogram for 67 iron meteorites corrected for pairing. After pairing correction, the data indicate 41 individual ejection events. The CRE ages are from this study, Lavielle et al. (1999), and Shankar et al. (2011).

group) indicate that this impact must had been massive. All other pairing cases contain fewer than five samples and, in most cases, fewer than three or two samples.

PERIODIC OR SUDDEN GCR VARIATIONS?

The major goal of this study is to explore whether or not the CRE age histogram for iron meteorites (Fig. 6) can provide any information about periodic and/or sudden GCR fluence variations. We first checked CRE age data for a periodicity of 134 Ma as proposed by Shaviv (2002, 2003). In Fig. 7, we plot the CRE ages as a function of the CRE with a modulo 134. In such a plot, it means that for data having a period of 134 Ma, the data group around a given x-value, which depends on the phase of the GCR oscillation, that is, the data group close to this x-value but spread over the entire range of CRE ages on the y-axis. The data, however, indicate differently; there is a large spread of data over the entire x-axis, indicating that there is no apparent periodicity. We found the same result for periods of 147 Ma (Scherer et al. 2006) and for 400 and 500 Ma (Alexeev 2016). Consequently, from our data, there is no indication for a periodicity in the CRE age data, which is in clear contradiction to the proposals by Shaviv (2002, 2003), Scherer et al. (2006), and Alexeev (2016). Furthermore, our result nicely confirms the earlier findings by Rahmstorf et al. (2004) and Jahnke (2005).

Going one step further, we can now compare our calculated CRE ages to available literature values for
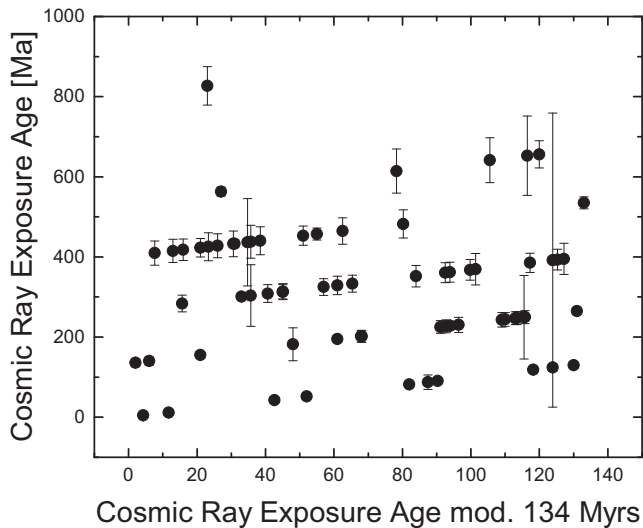
Fig. 7. Cosmic ray exposure ages as a function of the cosmic ray exposure ages modulo 134 Ma. The data show no indications for a 134 Ma periodicity. The CRE ages are from this study, Lavielle et al. (1999), and Shankar et al. (2011).

^{41}K-K CRE ages. In a previous study, Lavielle et al. (1999) highlighted a ~28% discrepancy between ^{36}Cl-^{36}Ar and ^{41}K-K CRE ages. The upper panel of Fig. 8 depicts the ^{41}K-K CRE ages for Ainsworth, Bendego, Bristol, Cape of Good Hope, Charlotte, Charlton, Grant, Hoba, Huizopa, Lombard, Merceditas, Morradal, Norfolk, Puente del Zacate, Sacramento Mountains, San Angelo, Sikhote-Alin, Tlacotepec, Treysa, Yanhuitlan, and Yardymly as a function of their ^{36}Cl-^{36}Ar CRE ages. The latter are from our study as well as from Lavielle et al. (1999) and Shankar et al. (2011). The ^{41}K-K CRE ages are from Voshage (1967). Unfortunately, from the 68 iron meteorites with reliable ^{36}Cl-^{36}Ar ages and the about 80 iron meteorites with ^{41}K-K ages, there are only 20 iron meteorites where we have both ^{36}Cl-^{36}Ar and ^{41}K-K ages. The solid black line is the 1:1 correlation, that is, data plotting close to this line are for meteorites with identical or very similar ^{36}Cl-^{36}Ar and ^{41}K-K ages.

The lower panel in Fig. 8 shows the ratio of ^{41}K-K CRE age to ^{36}Cl-^{36}Ar CRE as a function of the ^{36}Cl-^{36}Ar CRE age. Most of the ratios are higher than 1, indicating that the ^{41}K-K CRE ages are higher than the ^{36}Cl-^{36}Ar CRE ages. The average value considering all ratios is 1.41 ± 0.07, that is, significantly different from unity. The finding of systematic discrepancies can have two reasons: first, there might be an offset between both age systems. Remember that the ^{41}K-K CRE age system is based on relatively crude assumptions about the production rate ratios of potassium isotopes. The production rates of potassium isotopes are difficult to

model because there is little experimental data and nuclear model codes often fail to accurately describe production of magic or doubly magic isotopes, like the magic proton number ^{39}K, ^{40}K, and ^{41}K and the doubly magic nucleus ^{40}K. Second, it might also be that the observed systematic discrepancy indicates a change in the GCR fluence. The production rate ratio P(^{36}Cl)/P (^{36}Ar) = 0.835 used here to determine the CRE ages is based on the assumption of the same GCR fluence for ^{36}Cl and ^{36}Ar (e.g., Lavielle et al. 1999; Ammon et al. 2009). Radioactive ^{36}Cl reaches saturation after about 1.5 Ma and, therefore, only records the GCR fluence over the last 1.5 Ma. In contrast, ^{36}Ar production is over the entire CRE. A low ^{36}Cl-^{36}Ar CRE age can therefore indicate that the GCR fluence over the exposure time of the iron meteorite was lower than the GCR fluence over the last 1.5 Ma. The increase in the last 1.5 Ma would have essentially no effect on the ^{36}Ar budget considering that CRE ages are all in the range of a few hundred Ma. The data may therefore indicate that the GCR fluence over the time interval studied by us, that is, from 195 to 656 Ma, was lower by up to 40% compared to the currently assumed GCR fluence. This finding is in accord with the results by Lavielle et al. (1999). However, our value is slightly higher, that is, 40% compared to 28%, but is based on a significantly larger database for CRE ages.

From Fig. 8 one could also argue that there was a change in the cosmic ray flux 400 Ma ago. The ratio below 400 Ma is 1.52 ± 0.15, that is, different from unity by 3.4σ and the ratio above 400 Ma is 1.38 ± 0.07, that is, significantly different from one by 5.4σ. Although both values agree within the uncertainties, the ratios below 400 Ma scatter more than the values above 400 Ma. The meteorites with very high ratios, that is, large differences between ^{41}K-K and ^{36}Cl-^{36}Ar CRE ages are Bendego (2.77), Huizopa (1.74), Treysa (1.90), and Charlotte (1.52). We consider the ^{36}Cl-^{36}Ar CRE ages for all four meteorites reliable and there are also no indications for questioning the ^{41}K-K CRE ages. If the ratios were different for meteorites with short or long CRE ages, it might be possible to further pin down the time of the GCR fluence change (if there were any). With the current database, however, the uncertainties for the ^{41}K-K CRE ages are too large to firmly establish exactly when the GCR fluence changed.

We conclude that there are no periodic GCR intensity variations but that it is possible that the GCR intensity over the time interval from 195 Ma to 656 Ma was up to 40% lower than the GCR intensity over the last few Ma. Erlykin et al. (2009) argued that GCR intensity changes in the range ±1.5% can change the Earth temperature in the range ±0.07 °C, with a lower

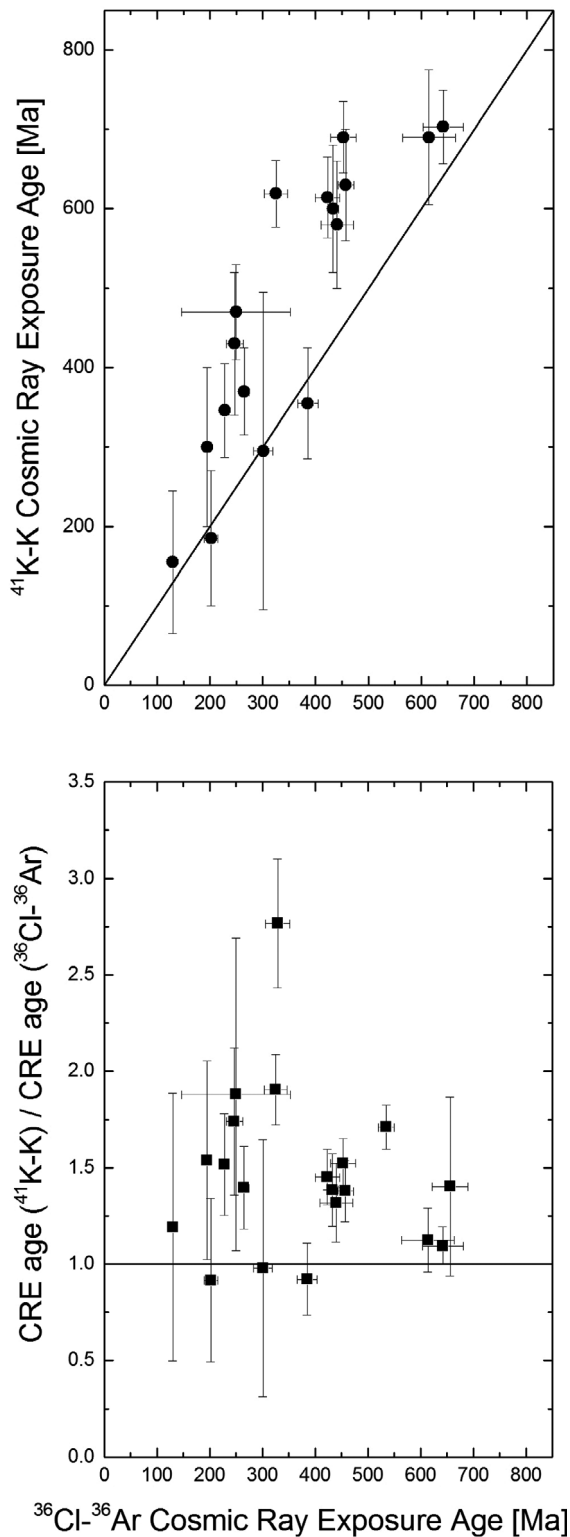Fig. 8. [41]K-K CRE ages as a function of [36]Cl-[36]Ar CRE ages (upper panel). Ratios of [41]K-K CRE ages/[36]Cl-[36]Ar CRE ages as function of [36]Cl-[36]Ar CRE ages (lower panel). The [36]Cl-[36]Ar CRE ages are from this study, Lavielle et al. (1999), and Shankar et al. (2011). The [41]K-K CRE ages are from Voshage (1967).

GCR flux corresponding to a higher temperature. Assuming a linear anticorrelation between GCR intensity and Earth climate, a change of 40% in the GCR intensity could change the Earth temperature by up to 2 °C. This being the case, the data would indicate that the Earth temperature in the time interval 195–656 Ma was ~2 °C higher than it was during the last few Ma (besides anthropogenic global warming). Temperature changes that large seem very unrealistic. We therefore speculate that the most likely explanation is a systematic bias between the [36]Cl-[36]Ar and the [41]K-K dating systems.

SUMMARY AND CONCLUSIONS

We measured the He, Ne, and Ar isotopic concentrations in 56 iron meteorites from six different groups (42 IIIABs, 7 IIABs, 3 IVAs, 1 IC, 1 IIA, 1 IIB, 1 ungrouped). In aliquots, we measured the Ni concentrations using ICP-MS and the [10]Be, [26]Al, [36]Cl, and [41]Ca radionuclide concentrations using AMS. From [41]Ca and [36]Cl activities together with model calculations (see Smith et al. 2017), we calculated terrestrial ages ranging from zero up to 562 ± 86 ka. The data confirm earlier results that terrestrial ages for iron meteorites can be as long as a few hundred thousand years even in relatively humid climate conditions (e.g., Chang and Wänke 1969; Aylmer et al. 1988; Smith et al. 2017).

The CRE ages were calculated using [36]Cl production rates, that is, the activity at the time of fall, and the cosmogenic [36]Ar concentrations. The ages range from 4.3 ± 0.4 Ma to 652 ± 99 Ma. By also considering recent data for the large iron meteorite Twannberg (Smith et al. 2017) and the data from Lavielle et al. (1999) and Shankar et al. (2011), we established a consistent and reliable CRE age database for 68 iron meteorites. At a first glance, the CRE age histogram shows peaks at about 400 and 630 Ma.

We corrected the data for pairing and concluded that, for example, 13 of the studied IIIAB iron meteorites were ejected in one single large impact event on the IIIAB parent body. After pairing correction, the database consists of 41 individual ejection events: 15 for the IIIAB iron meteorites, 7 for the IIAB meteorites, 4 for the IVAs, and 15 individual ejection events for all the other studied iron meteorites. The updated CRE age histogram shows no indications for periodic structures, especially not if one considers each group separately. Our data therefore confirm earlier results also arguing that the CRE age histogram for iron meteorites shows no indications for periodic GCR intensity variations (e.g., Rahmstorf et al. 2004; Jahnke 2005). In this respect, our data together with the other studies clearly contradict the hypothesis of periodic GCR intensity

variations as proposed by Shaviv (2002, 2003). However, the number of events is still too low to allow for statistically significant conclusions.

The ^{36}Cl-^{36}Ar ages determined by us and others are systematically lower than the ^{41}K-K CRE ages (e.g., Voshage 1967). The discrepancy is in the range 40%, which is in accord with earlier findings by Lavielle et al. (1999) and Ammon et al. (2009). A possible reason can simply be an offset in the ^{41}K-K dating system, which is not well constrained (e.g., Ammon et al. 2009). Another possible explanation is that there was a significant change in the GCR intensity with a 40% lower GCR flux in the time interval 195–656 Ma than over the last few Ma. Erlykin et al. (2009) argued that GCR intensity changes in the range ±1.5% can change the Earth temperature in the range ±0.07 °C. By assuming a linear dependence between GCR intensity and Earth temperature, a 40% lower GCR intensity could result in an Earth temperature about 2 °C higher. Temperature changes that large during this time period seem unrealistic. We conclude that the discrepancy, or at least a significant part of it, between the ^{41}K-K and ^{36}Cl-^{36}Ar CRE ages is caused by incorrect assumptions in the ^{41}K-K dating system. Before we can safely conclude whether or not there was a GCR intensity change, there is a need to better understand and probably also to improve the ^{41}K-K dating system.

Editorial Handling—Dr. Marc Caffee

REFERENCES

Akhmadaliev S., Heller R., Hanf D., Rugel G., and Merchel S. 2013. The new 6 MV AMS-facility DREAMS at Dresden. *Nuclear Instruments and Methods in Physics Research B* 294:5–10.

Alexeev V. A. 2016. Long-term galactic cosmic ray variations over the last billion years based on the cosmic-ray exposure of iron meteorites. *Geochemistry International* 54:78–84.

Ammon K., Masarik J., and Leya I. 2008. Noble gases in Grant and Carbo and the influence of S- and P-rich mineral inclusions on the ^{41}K-^{40}K dating system. *Meteoritics & Planetary Science* 43:685–699.

Ammon K., Masarik J. and Leya I. 2009. New model calculations for the production rates of cosmogenic nuclides in iron meteorites. *Meteoritics & Planetary Science* 44:485–503.

Ammon K., Leya I., and Lin Y. 2011. Noble gases in the Xinjiang (Armanty) iron meteorite—A big object with a short cosmic-ray exposure age. *Meteoritics & Planetary Science* 46:785–792.

Artamonova I., and Veretenenko S. 2011. Galactic cosmic ray variation influence on baric system dynamics at middle latitudes. *Journal of Atmospheric and Solar-Terrestrial Physics* 73:36–370.

Aylmer D., Bonnano V., Herzog G. F., Klein J., and Middleton R. 1988. ^{26}Al and ^{10}Be production in iron meteorites. *Earth and Planetary Science Letters* 88:107–118.

Bajo K., Nagao K., and Honda M. 2008. Noble gases in a Gibeon iron meteorite fragment heavily shielded to cosmic-rays. 71st Annual Meeting of the Meteoritical Society. Abstract #5073.

Begemann F., Weber H. W., Vilcsek E., and Hintenberger H. 1976. Rare gases and ^{36}Cl in stony-iron meteorites: cosmogenic elemental production rates, exposure ages, diffusion losses and thermal histories. *Geochimica et Cosmochimica Acta* 40:353–368.

Chang C. and Wänke H. 1969. Beryllium-10 in iron meteorites, their cosmic-ray exposure and terrestrial ages. In *Meteorite research*, edited by Millman P. M. Dordrecht, the Netherlands: Reidel Publishing Company. pp. 397–406.

Drimmel R. 2000. Evidence for a two-armed spiral in the Milky Way. *Astronomy and Astrophysics* 258:L13–L16.

Erlykin A. D., Sloan T., and Wolfendale A. W. 2009. Solar activity and the mean global temperature. *Environmental Research Letters* 4:014006. https://doi.org/10.1088/1748-9326/4/1/014006.

Erlykin A. D., Sloan T., and Wolfendale A. W. 2010. Correlations of clouds, cosmic rays and solar irradiation over the Earth. *Journal of Atmospheric and Solar-Terrestrial Physics* 72:151–156.

Frigo E., Pacca I. G., Pereira-Filho A. J., Rampelloto P. H., and Rigozo N. R. 2013. Evidence for cosmic ray

modulation in temperature records from the South Atlantic Magnetic Anomaly region. *Annales Geophysicae* 31:1833–1841.

Gies D. R. and Helsel J. W. 2005. Ice age epochs and Sun's path through the galaxy. *The Astrophysical Journal* 626:844–848.

Hampel W. and Schaeffer O. A. 1979. ^{26}Al in iron meteorites and the constancy of cosmic ray intensity in the past. *Earth and Planetary Science Letters* 42:348–358.

Honda M., Caffee M. W., Miura Y. N., Nagai H., Nagao K., and Nishiizumi K. 2002. Cosmogenic nuclides in the Brenham pallasite. *Meteoritics & Planetary Science* 37:1711–1728.

Honda M., Nagai H., Nagao K., Bajo K., and Oura Y. 2008. Cosmogenic histories in Gibeon and Campo Del Cielo iron meteorites. 71st Annual Meeting of the Meteoritical Society. Abstract #5047.

Jahnke K. 2005. On the periodic clustering of cosmic ray exposure ages of iron meteorites. *Astronomy and Astrophysics* No. 4155J. http://tinyurl.com/388odc.

Jörg G., Amelin Y., Kossert K., and Gostomski C. L. 2012. Precise and direct determination of the half-life of ^{41}Ca. *Geochimica et Cosmochimica Acta* 88:51–65.

Kirkby J. 2007. Cosmic rays and climate. *Surveys in Geophysics* 28:333–375.

Korschinek G., Bergmaier A., Faestermann T., Gerstmann U. C., Knie K., Rugel G., Wallner A., Dillmann I., Dollinger G., Lierse von Gostomski Ch., Kossert K., Maiti M., Poutivtsev M., and Remmert A. 2010. A new value for the half-life of ^{10}Be by heavy-ion elastic recoil detection and liquid scintillation counting. *Nuclear Instruments and Methods in Physics Research* B268:187–191.

Kristjánsson J. E., Staple A., and Kristiansen J. 2002. A new look at possible connection between solar activity, clouds and climate. *Geophysical Research Letters* 29:22-1–22-4.

Kutschera W., Ahmad I., and Paul M. 1992. Half-Life determination of ^{41}Ca and some other radioisotopes. *Radiocarbon* 34:436–446.

Laut P. 2003. Solar activity and terrestrial climate: An analysis of some purported correlations. *Journal of Atmospheric and Solar-Terrestrial Physics* 65:801–812.

Lavielle B., Nishiizumi K., Marti K., Jeannot J.-P., Caffee M. W., and Finkel R. C. 1995. Depth-dependent concentrations of cosmogenic ^{10}Be, ^{26}Al, ^{36}Cl, He$_c$, Ne$_c$, and Ar$_c$ in the Old Woman iron meteorite. *Meteoritics* 30:534.

Lavielle B., Marti K., Jeannot J.-P., Nishiizumi K., and Caffee M. 1999. The ^{36}Cl–^{36}Ar–^{40}K–^{41}K records and cosmic ray production rates in iron meteorites. *Earth and Planetary Science Letters* 170:93–104.

Lipschutz M. E., Signer P., and Anders E. 1965. Cosmic ray exposure ages of iron meteorites by the ^{21}Ne/^{26}Al method. *Journal of Geophysical Research* 70:1473–1489.

Merchel S. and Herpers U. 1999. An update on radiochemical separation techniques for the determination of long-lived radionuclides via accelerator mass spectrometry. *Radiochimica Acta* 84:215–219.

Merchel S., Bremser W., Alfimov V., Arnold M., Aumaître G., Benedetti L., Bourlès D. L., Caffee M., Fifield L. K., Finkel R. C., Freeman S. P. H. T., Martschini M., Matsushi Y., Rood D. H., Sasa K., Steier P., Takahashi T., Tamari M., Tims S. G., Tosaki Y., Wilcken K. M., and Xu S. 2011. Ultra-trace analysis of ^{36}Cl by accelerator mass spectrometry: an interlaboratory study. *Analytical and Bioanalytical Chemistry* 400:3125–3132.

Michlovich E. S., Vogt S., Masarik J., Reedy R. C., Elmore D., and Lipschutz M. E. 1994. Aluminum 26, ^{10}Be, and ^{36}Cl depth profiles in the Canyon Diablo iron meteorite. *Journal of Geophysical Research* 99:23,187–23,194.

Nica N., Cameron J., and Balraj S. 2012. Nuclear data sheets for A=36. *Nuclear Data Sheets* 113:1–115.

Nishiizumi K., Okazaki R., Park J., Nagao K., Masarik J., and Finkel R. C. 2002. Exposure and terrestrial histories of Dhofar 019 Martian meteorite (abstract #1355). 33rd Lunar and Planetary Science Conference. CD-ROM.

Ormes J. F. 2017. Cosmic rays and climate. *Advances in Space Research* 10:2880–2891. https://doi.org/10.1016/j.asr.2017.07.028.

Overholt A. C., Melott A. L., and Pohl M. 2009. Testing the link between terrestrial climate change and galactic spiral arm transit. *The Astronomical Journal* 705:L101–L103.

Pavetich S., Akhmadaliev S., Arnold M., Aumaître G., Bourlès D., Buchriegler J., Golser R., Keddadouche K., Martschini M., Merchel S., Rugel G., and Steier P. 2016. Interlaboratory study of the ion source effect in ^{36}Cl accelerator mass spectrometry. *Nuclear Instruments and Methods in Physics Research B* 329:22–29.

Rahmstorf S., Archer D., Ebel D. S., Eugster O., Jouzel J., Maraun D., Neu U., Schmidt G., Severinghaus J., Weaver A. J., and Zachos J. 2004. Cosmic rays, carbon dioxide, and climate. *Eos* 85:1739–1746.

Rugel G., Pavetich S., Akmadaliev S., Baez S. M. E., Scharf A., Ziegenrücker R., and Merchel S. 2016. The first four years of the AMS-facility DREAMS: status and developments for more accurate radionuclide data. *Nuclear Instruments and Methods in Physics Research B* 370:94–100.

Schaeffer O. A. and Heymann D. 1965. Comparison of Cl^{36}-Ar^{36} and Ar^{39}-Ar^{38} cosmic ray exposure ages of dated fall iron meteorites. *Journal of Geophysical Research* 70:215–224.

Scherer K., Fichtner H., Borrmann T., Beer J., Desorgher L., Flückiger E., Fahr H. J., Ferreira S. E. S., Langner U. W., Potgieter M. S., Heber B., Masarik J., and Shaviv N. J. 2006. Interstellar terrestrial relations: variable cosmic environments, the dynamic heliosphere, and their imprints on terrestrial archives and climate. *Space Science Reviews* 127:327–465.

Shankar N. 2011. Cosmic ray exposure ages of iron meteorites using ^{39}K-^{40}K-^{41}K dating. Dissertation, Rutgers, New Brunswick, New Jersey, USA.

Shankar N., Rugel G., Faestermann T., Korschinek G., Swisher III C C., Turrin B., Herzog G. F., and Walker R. J. 2011. ^{10}Be, ^{26}Al, and ^{36}Cl in iron meteorites: Implications for osmium isotope systematics (abstract #1262). 42nd Lunar and Planetary Science Conference. CD-ROM.

Shaviv N. J. 2002. Cosmic ray diffusion from the galactic spiral arms, iron meteorites, and a possible climatic connection? *Physical Review Letters* 89:0511021.

Shaviv N. J. 2003. The spiral structure of the Milky Way, cosmic rays, and ice age epochs on Earth. *New Astronomy* 8:39–77.

Sloan T. 2013. Cosmic rays, solar activity and the climate. 23rd European Cosmic Ray Conference. *Journal of Physics: Conference Series* 409:012020. https://doi.org/10.1088/1742-6596/409/1/012020.

Sloan T. and Wolfendale A. W. 2008. Testing the proposed causal link between cosmic rays and cloud cover.

Environmental Research Letters 3:024001. https://doi.org/10.1088/1748-9326/3/2/024001.

Sloan T. and Wolfendale A. W. 2013a. Cosmic rays, solar activity and the climate. *Environmental Research Letters* 8:045022. https://doi.org/10.1088/17748-9326/8/4/045022.

Sloan T. and Wolfendale A. W. 2013b. Cosmic rays and climate change of the past 1000 million years. *New Astronomy* 25:45–49.

Smith T., Hofmann B. A., Leya I., Merchel S., Pavetich S., Rugel G., and Scharf A. 2017. The cosmic-ray exposure history of the Twannberg iron meteorite (IIG). *Meteoritics & Planetary Science* 52:2241–2257.

Svensmark H. 1998. Influence of cosmic rays on Earth's climate. *Physical Review* 81:5027–5030.

Svensmark H. and Friis-Christensen E. 1997. Variation of cosmic ray flux and global could coverage – a missing link in solar-climate relationships. *Journal of Atmospheric and Solar-Terrestrial Physics* 59:1225–1232.

Vallée J. P. 2017. A guided map to the spiral arms in the galactic disk of the Milky Way. *Astronomical Review* 13:113–146.

Voshage H. 1967. Bestrahlungsalter und Herkunft der Eisenmeteorite. *Zeitschrift für Naturforschung* 22a:477–506.

Voshage H. and Feldmann H. 1978. Investigations on cosmic-ray-produced nuclides in iron meteorites, 2. New results on ^{41}K/^{40}K-^{4}He/^{21}Ne exposure ages and the interpretation of age distribution. *Earth and Planetary Science Letter* 40:83–90.

Voshage H. and Feldmann H. 1979. Exposure ages, meteoroid sizes and sample depths determined by mass spectrometric analyses of potassium and rare gases. *Earth and Planetary Science Letter* 45:293–308.

Wallmann K. 2004. Impact of atmospheric CO_2 and galactic cosmic radiation on Phanerozoic climate change and the marine $\delta^{18}O$ record. *Geochemistry, Geophysics, Geosystems* 5:Q06004. https://doi.org/10.1029/2003GC000683.

Wieler R. 2002. Noble gases in the solar system. *Reviews in Mineralogy and Geochemistry* 47:21–70.

Wieler R., Beer J., and Leya I. 2013. The galactic cosmic ray intensity over the past 10^6-10^9 years as recorded by cosmogenic nuclides in meteorites and terrestrial samples. *Space Science Reviews* 176:351–363.

Xue S., Herzog G. F., Souzis A., Ervin M. H., Lareau R. T., Middleton R., and Klein J. 1995. Stable magnesium isotopes, ^{26}Al, ^{10}Be, and ^{26}Mg/^{26}Al exposure ages of iron meteorites. *Earth and Planetary Science Letters* 136:397–406.

APPENDIX A

Table A1. Collections and museums from which the studied samples were obtained together with the known found mass (kg, in parentheses).

Name of collection/Museum	Meteorite (found mass in kg)
Edge University/Turkey	Kayakent (85)
The Natural History Museum/London/UK	Avoca (37.85), Fort Pierre (15.9), Greenbrier County (5), Joel's Iron (1.3), Mapleton (49), Norfolk (23), Rowton (3.5), Schwetz (21.5), Treysa (63), Verkhne Udinsk (18)
Collection at University of Bern/Switzerland	Arispe (683), Bristol (20), Brownfield (1.63), Calico Rock (7.28), Cape York (58.2 t), Casas Grandes (1.55 t), Gan Gan (83), Gibeon (26 t), Grant (525), Lombard (7), Pinon (17.85), Squaw Creek (14.5), Trenton (505)
Vienna Natural History Museum/Austria	Carthage (127), Charcas (1.4 tons), Chulafinnee (16.22), Dalton (53), Durango (164), Plymouth (14)
The Field Museum, Chicago/USA	Costilla Peak (35.5), Davis Mountains (689), Kenton County (194), La Porte (14.54), Sandtown (9.35)
Royal Ontario Museum/Canada	Durango (164), Puente del Zacate (30.79), Sacramento Mountains (237.2), San Angelo (88)
Centre Européen de Recherche et d'Enseignement en Géoscience de l'Environnement/France	Bur-Abor (290), Catalina 107 (0.5), Djebel-in-Azzene (12.5), Henbury (2 t), NWA 8442 (2.23), Roebourne (86.86), Tamentit (510), Zerhamra (630)
Senckenberg Natural History Museum, Frankfurt am Main/Germany	Benedict (16.38), Boxhole (500), Elyria (10.9), Nazareth (11.31), Picacho (22), Turtle River (22.39)
American Museum of Natural History (via D. Cook)	Braunau (39), Cincinnati (1.5), Forsyth County (22.7),
Collection at ETH Zurich, Switzerland	North Chile (300), Sikhote-Alin (23 t)

Table A2. He, Ne, and Ar concentrations (in 10^{-8} cm^3 STP per g) and isotopic compositions in the analyzed IIIAB iron meteorites.

Sample	Type	^{4}He	^{4}He/^{3}He	^{20}Ne	^{20}Ne/^{22}Ne	^{22}Ne/^{21}Ne	^{38}Ar	^{36}Ar/^{38}Ar	^{40}Ar/^{36}Ar
Avoca	IIIAB	2273 ± 23	3.58 ± 0.01	7.985 ± 0.046	0.893 ± 0.004	1.039 ± 0.005	37.4 ± 1.3	0.656 ± 0.034	12 ± 1
Arispe	IC	72.7 ± 0.7	4.04 ± 0.01	0.207 ± 0.004	0.911 ± 0.034	1.088 ± 0.005	0.862 ± 0.031	0.944 ± 0.049	114 ± 7
Benedict	IIIAB	1167 ± 12	1.94 ± 0.01	6.696 ± 0.059	0.892 ± 0.001	1.041 ± 0.001	38.8 ± 1.4	0.640 ± 0.033	12 ± 1
Boxhole	IIIAB	96.8 ± 1.0	4.20 ± 0.01	0.555 ± 0.004	1.053 ± 0.007	1.077 ± 0.006	0.180 ± 0.01	1.036 ± 0.054	149 ± 9
Braunau	IIAB	61.1 ± 0.6	12.89 ± 0.02	0.174 ± 0.004	0.912 ± 0.036	1.034 ± 0.011	0.983 ± 0.034	1.113 ± 0.059	143 ± 9
Bristol	IVA	n.d.	n.d.	4.893 ± 0.099	0.903 ± 0.034	1.031 ± 0.001	20.5 ± 0.9	0.689 ± 0.036	17 ± 1
Brownfield	IIB	n.d.	n.d.	4.260 ± 0.086	0.906 ± 0.034	1.037 ± 0.001	17.4 ± 0.6	0.678 ± 0.035	15 ± 1
Bur-Abor	IIIAB	1603 ± 17	3.66 ± 0.01	4.825 ± 0.017	0.888 ± 0.002	1.040 ± 0.001	23.9 ± 0.8	0.660 ± 0.034	20 ± 1
Cape York	IIIAB	69.4 ± 2.7	6.49 ± 0.01	0.163 ± 0.002	1.045 ± 0.011	1.050 ± 0.007	0.808 ± 0.028	1.164 ± 0.061	150 ± 9
Calico Rock	IIA	n.d.	n.d.	4.836 ± 0.099	0.894 ± 0.033	1.038 ± 0.001	27.8 ± 1.0	0.637 ± 0.033	10 ± 1
Carthage	IIIAB	503 ± 6	4.07 ± 0.02	1.208 ± 0.009	0.902 ± 0.006	1.047 ± 0.005	0.005 ± 0.001	4.534 ± 0.397	256 ± 16
Casas Grandes	IIIAB	226 ± 2	4.09 ± 0.01	0.411 ± 0.002	0.902 ± 0.004	1.047 ± 0.003	2.61 ± 0.09	0.728 ± 0.038	57 ± 3
Catalina 107	IIIAB	1828 ± 18	3.27 ± 0.01	6.641 ± 0.034	0.952 ± 0.002	1.045 ± 0.001	25.4 ± 0.9	0.686 ± 0.036	28 ± 2
Charcas	IIIAB	675 ± 7	3.78 ± 0.01	2.487 ± 0.013	1.145 ± 0.005	1.077 ± 0.003	10.2 ± 0.4	0.677 ± 0.035	28 ± 2
Chulafinnee	IIIAB	1329 ± 13	3.43 ± 0.01	4.342 ± 0.019	0.898 ± 0.003	1.037 ± 0.003	21.3 ± 0.7	0.649 ± 0.034	13 ± 1
Cincinnati	IIAB	831 ± 9	3.00 ± 0.01	3.770 ± 0.078	0.901 ± 0.034	1.034 ± 0.001	17.4 ± 0.6	0.687 ± 0.036	19 ± 1
Costilla Peak	IIIAB	1604 ± 16	3.01 ± 0.01	6.424 ± 0.017	0.905 ± 0.001	1.036 ± 0.001	24.1 ± 0.8	0.676 ± 0.035	11 ± 1
Dalton	IIIAB	1027 ± 10	3.75 ± 0.01	3.221 ± 0.012	0.889 ± 0.003	1.040 ± 0.004	15.7 ± 0.54	0.676 ± 0.035	28 ± 2
Davis Mountains	IIIAB	1250 ± 13	2.88 ± 0.01	4.347 ± 0.005	0.892 ± 0.001	1.037 ± 0.001	21.6 ± 0.7	0.647 ± 0.034	10 ± 1
Djebel-in-Azzene	IIIAB	2016 ± 20	3.18 ± 0.01	7.357 ± 0.058	0.910 ± 0.001	1.034 ± 0.001	32.0 ± 1.1	0.648 ± 0.034	8 ± 1
Durango	IIIAB	1351 ± 14	3.90 ± 0.01	3.908 ± 0.018	0.898 ± 0.004	1.037 ± 0.002	19.2 ± 0.7	0.652 ± 0.034	18 ± 1
Elyria	IIIAB	1240 ± 12	2.44 ± 0.01	5.995 ± 0.022	0.890 ± 0.001	1.039 ± 0.001	3.47 ± 0.12	0.644 ± 0.034	12 ± 1
Forsyth County	IIAB	159 ± 2	3.45 ± 0.02	0.583 ± 0.013	0.897 ± 0.034	1.042 ± 0.006	3.08 ± 0.11	0.868 ± 0.045	91 ± 5
Fort Pierre	IIIAB	n.d.	n.d.	6.393 ± 0.028	0.903 ± 0.001	1.037 ± 0.001	26.3 ± 0.9	0.661 ± 0.034	8 ± 1
Gan Gan	IVA	n.d.	n.d.	3.603 ± 0.074	0.902 ± 0.034	1.041 ± 0.002	17.1 ± 0.6	0.663 ± 0.035	19 ± 1
Gibeon		72.2 ± 0.7	6.45 ± 0.01	0.128 ± 0.003	1.078 ± 0.040	1.059 ± 0.009	0.413 ± 0.026	1.906 ± 0.107	201 ± 12
Grant	IIIAB	87.5 ± 1.8	n.d.	5.10 ± 0.03	0.863 ± 0.030	1.08 ± 0.03	33.48 ± 1.15	0.68 ± 0.04	8.27 ± 0.44
Greenbrier County	IIIAB	110 ± 1	1.95 ± 0.01	0.638 ± 0.002	0.895 ± 0.001	1.037 ± 0.001	3.41 ± 0.12	0.641 ± 0.033	9 ± 1
Henbury	IIIAB	540 ± 5	4.07 ± 0.01	1.770 ± 0.013	0.908 ± 0.006	1.043 ± 0.004	7.54 ± 0.26	0.749 ± 0.039	54 ± 3
Joel's Iron	IIIAB	156 ± 2	3.31 ± 0.01	0.634 ± 0.002	0.891 ± 0.001	1.039 ± 0.001	3.36 ± 0.12	0.666 ± 0.035	21 ± 1
Kayakent	IIIAB	178 ± 2	3.13 ± 0.01	0.747 ± 0.001	0.899 ± 0.001	1.039 ± 0.001	3.87 ± 0.14	0.661 ± 0.034	16 ± 1
Kenton County	IIIAB	1738 ± 18	3.65 ± 0.01	4.338 ± 0.016	0.896 ± 0.003	1.040 ± 0.005	22.5 ± 0.8	0.655 ± 0.034	14 ± 1
La Porte	IIIAB	911 ± 10	4.26 ± 0.04	2.089 ± 0.019	0.884 ± 0.006	1.044 ± 0.008	10.6 ± 0.4	0.670 ± 0.035	24 ± 1
Lombard	IIAB	62.3 ± 0.6	4.51 ± 0.01	0.188 ± 0.004	0.980 ± 0.039	1.114 ± 0.008	0.724 ± 0.030	1.119 ± 0.059	143 ± 9
Mapleton	IIIAB	n.d.	n.d.	2.927 ± 0.013	0.895 ± 0.002	1.041 ± 0.002	18.7 ± 0.6	0.641 ± 0.033	14 ± 1
Nazareth	IIIAB	1539 ± 15	2.77 ± 0.01	6.298 ± 0.038	0.892 ± 0.001	1.032 ± 0.002	3.72 ± 0.14	0.658 ± 0.034	20 ± 1
Norfolk	IIAB	n.d.	n.d.	6.465 ± 0.032	0.921 ± 0.001	1.041 ± 0.005	n.d.	n.d.	n.d.
North Chile	IIAB	207 ± 2	6.44 ± 0.01	0.423 ± 0.009	0.885 ± 0.034	1.054 ± 0.007	2.18 ± 0.08	0.919 ± 0.048	111 ± 7
NWA 8442	IIIAB	334 ± 3	4.60 ± 0.01	0.967 ± 0.008	0.897 ± 0.006	1.037 ± 0.001	4.53 ± 0.16	0.760 ± 0.040	59 ± 3
Picacho	IIIAB	1705 ± 17	3.35 ± 0.01	5.403 ± 0.027	0.893 ± 0.001	1.037 ± 0.007	35.0 ± 1.2	0.658 ± 0.034	25 ± 1
Pinon	Ungr.	102 ± 1	3.96 ± 0.01	0.333 ± 0.007	0.940 ± 0.035	1.072 ± 0.005	1.49 ± 0.06	0.838 ± 0.044	85 ± 5
Plymouth	IIIAB	1873 ± 23	3.18 ± 0.03	7.474 ± 0.063	0.896 ± 0.006	1.040 ± 0.004	31.8 ± 1.1	0.669 ± 0.035	16 ± 1

Table A2. *Continued.* He, Ne, and Ar concentrations (in $10^{-8} cm^3$ STP per g) and isotopic compositions in the analyzed IIIAB iron meteorites.

Sample	Type	^4He	$^4He/^3He$	^{20}Ne	$^{20}Ne/^{22}Ne$	$^{22}Ne/^{21}Ne$	^{38}Ar	$^{36}Ar/^{38}Ar$	$^{40}Ar/^{36}Ar$
Puente del Zacate	IIIAB	1943 ± 20	3.43 ± 0.01	6.526 ± 0.029	0.889 ± 0.003	1.040 ± 0.010	31.9 ± 1.1	0.651 ± 0.034	14 ± 1
Roebourne	IIIAB	696 ± 8	3.44 ± 0.02	2.236 ± 0.023	0.895 ± 0.007	1.040 ± 0.001	9.70 ± 0.33	0.674 ± 0.035	23 ± 1
Rowton	IIIAB	n.d.	n.d.	4.026 ± 0.012	0.899 ± 0.001	1.040 ± 0.001	18.7 ± 0.7	0.672 ± 0.036	20 ± 1
Sacramento Mountains	IIIAB	902 ± 9	3.38 ± 0.03	3.510 ± 0.016	0.953 ± 0.002	1.041 ± 0.001	13.6 ± 0.5	0.678 ± 0.035	19 ± 1
San Angelo	IIIAB	1025 ± 11	3.74 ± 0.02	2.835 ± 0.012	0.955 ± 0.003	1.052 ± 0.004	14.9 ± 0.5	0.651 ± 0.034	22 ± 1
Sandtown	IIIAB	2070 ± 21	3.34 ± 0.11	8.618 ± 0.019	0.903 ± 0.001	1.035 ± 0.001	37.6 ± 1.3	0.652 ± 0.034	5 ± 1
Schwetz	IIIAB	207 ± 2	1.63 ± 0.01	1.611 ± 0.007	1.052 ± 0.003	1.064 ± 0.003	6.82 ± 0.24	0.711 ± 0.037	48 ± 3
Sikhote-Alin	IIAB	847 ± 9	3.68 ± 0.01	2.178 ± 0.045	0.867 ± 0.032	1.052 ± 0.004	10.7 ± 0.4	0.685 ± 0.035	19 ± 1
Squaw Creek	IIAB	53.1 ± 0.5	9.18 ± 0.02	0.119 ± 0.003	1.273 ± 0.056	1.115 ± 0.015	0.506 ± 0.021	1.636 ± 0.086	207 ± 12
Tamentit	IIIAB	1840 ± 19	3.18 ± 0.01	7.060 ± 0.041	0.979 ± 0.002	1.044 ± 0.002	29.2 ± 1.0	0.644 ± 0.034	6 ± 1
Trenton	IIIAB	1435 ± 16	3.76 ± 0.02	3.900 ± 0.024	0.884 ± 0.004	1.045 ± 0.005	0.004 ± 0.001	2.948 ± 0.270	278 ± 22
Treysa	IIIAB	n.d.	n.d.	5.878 ± 0.010	0.910 ± 0.001	1.038 ± 0.001	25.1 ± 0.9	0.653 ± 0.034	11 ± 1
Turtle River	IIIAB	1049 ± 11	3.11 ± 0.01	4.423 ± 0.024	0.892 ± 0.004	1.040 ± 0.005	19.7 ± 0.7	0.655 ± 0.034	8 ± 1
Verkhne Udinsk	IIIAB	n.d.	n.d.	5.434 ± 0.020	0.933 ± 0.001	1.043 ± 0.002	32.1 ± 1.1	0.668 ± 0.035	7 ± 1
Zerhamra	IIIAB	447 ± 5	3.60 ± 0.01	1.757 ± 0.013	0.897 ± 0.005	1.037 ± 0.006	8.75 ± 0.30	0.678 ± 0.035	22 ± 1

The given uncertainties are only the uncertainties due to ion counting statistics, blank corrections, interference corrections, and to the extrapolation of the measured signal to the time of gas inlet into the spectrometer. Since noble gas mass spectrometers are optimized for isotope ratio measurements, the uncertainties caused by the extrapolation are very often much smaller for isotope ratios than for individual isotopes.

Table A3. Radionuclide activities [dpm/kg] calculated from isotopic ratios measured by AMS and Ni concentrations (%).

Meteorite	Group	^{10}Be	^{26}Al	^{36}Cl	^{41}Ca	Ni
Avoca	IIIAB	4.06 ± 0.08	2.933 ± 0.063	18.77 ± 0.24	17.57 ± 0.91	8.82
Arispe	IC	0.92 ± 0.02	0.723 ± 0.022	Sample lost	$4.04^{+1.77}_{-1.35}$	6.20
Benedict	IIIAB	5.02 ± 0.10	3.769 ± 0.132	24.38 ± 0.40	28.50 ± 1.12	8.85
Boxhole	IIIAB	0.164 ± 0.04	0.148 ± 0.010	1.002±0.076	1.65 ± 0.18	7.30
Braunau	IIAB	3.66 ± 0.07	2.766 ± 0.070	20.13 ± 0.23	22.25 ± 1.05	5.11
Bristol	IVA	3.52 ± 0.07	2.022 ± 0.046	7.157±0.166	$0.79^{+0.65}_{-0.51}$	8.49
Brownfield	IIB	5.24 ± 0.10	3.715 ± 0.088	19.63 ± 0.73	24.50 ± 2.72	10.31
Bur-Abor	IIIAB	3.33 ± 0.07	2.333 ± 0.051	15.48 ± 0.23	14.75 ± 0.56	7.63
Cape York	IIIAB	0.087 ± 0.002	0.095 ± 0.006	0.431±0.017	$0.36^{+0.69}_{-0.32}$	8.38
Calico Rock	IIA	5.57 ± 0.11	3.330 ± 0.074	14.43 ± 0.35	8.84 ± 1.39	5.58
Carthage	IIIAB	1.55 ± 0.03	1.066 ± 0.038	5.160±0.058	1.37 ± 0.20	11.11
Casas Grandes	IIIAB	0.56 ± 0.01	0.290 ± 0.020	0.847±0.073	0.31 ± 0.14	7.73
Catalina 107	IIIAB	4.51 ± 0.09	3.588 ± 0.111	21.42 ± 0.28	26.08 ± 1.15	11.08
Charcas	IIIAB	1.45 ± 0.03	1.115 ± 0.042	7.307±0.082	5.09 ± 0.35	8.60
Chulafinnee	IIIAB	4.64 ± 0.09	3.298 ± 0.105	21.78 ± 0.24	22.40 ± 0.79	10.50
Cincinnati	IIAB	5.52 ± 0.10	3.897 ± 0.090	20.46 ± 0.22	17.74 ± 0.80	8.70
Costilla Peak	IIIAB	5.37 ± 0.11	3.683 ± 0.066	21.97 ± 0.32	25.27 ± 0.74	7.57
Dalton	IIIAB	3.30 ± 0.06	2.370 ± 0.082	16.47 ± 0.19	15.77 ± 0.68	12.57
Davis Mountains	IIIAB	2.69 ± 0.05	1.921 ± 0.043	13.84 ± 0.22	15.80 ± 0.61	7.54
Djebel-in-Azzene	IIIAB	5.26 ± 0.10	3.909 ± 0.111	13.05 ± 0.18	6.15 ± 0.57	8.08
Durango	IIIAB	1.69 ± 0.03	1.250 ± 0.053	10.02 ± 0.11	5.67 ± 0.41	10.90
Elyria	IIIAB	5.05 ± 0.10	3.617 ± 0.087	24.17 ± 0.27	25.50 ± 1.01	8.68
Forsyth County	IIAB	3.80 ± 0.07	2.661 ± 0.066	12.03 ± 0.13	5.80 ± 0.44	5.03
Fort Pierre	IIIAB	5.23 ± 0.10	3.624 ± 0.067	21.62 ± 0.31	28.08 ± 1.03	7.52
Gan Gan	IVA	3.38 ± 0.07	2.514 ± 0.053	Sample lost	19.17 ± 1.98	9.51
Gibeon	IVA	bdl	bdl	bdl	n.d.	8.37
Grant	IIIAB	Sample lost	2.214 ± 0.066	14.28 ± 0.16	15.54 ± 0.83	7.17
Greenbrier County	IIIAB	4.03 ± 0.08	2.901 ± 0.074	25.44 ± 0.33	22.02 ± 0.84	6.85
Henbury	IIIAB	0.018 ± 0.001	0.014 ± 0.003	0.068±0.004	0.32 ± 0.16	3.33
Joel's Iron	IIIAB	4.59 ± 0.09	3.147 ± 0.069	19.11 ± 0.24	19.53 ± 2.61	8.74
Kayakent	IIIAB	4.32 ± 0.09	2.822 ± 0.074	19.83 ± 0.37	36.57 ± 5.03	7.28
Kenton County	IIIAB	1.83 ± 0.04	0.887 ± 0.022	2.571±0.041	0.224±0.061	6.78
La Porte	IIIAB	4.63 ± 0.09	3.198 ± 0.061	19.11 ± 0.29	19.32 ± 0.70	8.16
Lombard	IIAB	0.54 ± 0.01	0.428 ± 0.016	3.116±0.066	3.52 ± 0.57	5.42
Mapleton	IIIAB	3.92 ± 0.07	2.835 ± 0.055	19.49 ± 0.25	22.97 ± 0.98	7.52
Nazareth	IIIAB	1.47 ± 0.06	3.242 ± 0.134	22.67 ± 0.26	25.96 ± 1.09	9.37
Norfolk	IIIAB	5.16 ± 0.10	3.481 ± 0.070	20.55 ± 0.57	23.09 ± 4.22	7.14
North Chile	IIAB	1.06 ± 0.02	0.560 ± 0.020	1.673±0.022	0.140±0.055	5.23
NWA 8442	IIIAB	2.42 ± 0.05	1.578 ± 0.039	11.92 ± 0.19	11.49 ± 0.62	5.93
Picacho	IIIAB	3.93 ± 0.08	2.630 ± 0.138	16.66 ± 0.28	12.28 ± 0.73	7.44
Piñon	Ungr.	3.63 ± 0.07	2.038 ± 0.048	Sample lost	$1.53^{+0.82}_{-0.58}$	16.57
Plymouth	IIIAB	4.84 ± 0.09	3.184 ± 0.132	22.73 ± 0.26	23.98 ± 0.81	11.52
Puente del Zacate	IIIAB	3.13 ± 0.06	1.799 ± 0.070	7.135±0.093	2.18 ± 0.26	8.54
Roebourne	IIIAB	4.39 ± 0.08	3.407 ± 0.108	20.12 ± 0.22	19.90 ± 0.77	9.04
Rowton	IIIAB	5.00 ± 0.10	3.447 ± 0.078	21.20 ± 0.33	23.23 ± 2.14	7.04
Sacramento Mountains	IIIAB	3.62 ± 0.07	2.227 ± 0.067	12.95 ± 0.17	7.50 ± 0.45	7.74
San Angelo	IIIAB	1.52 ± 0.03	1.032 ± 0.034	6.845 ± 0.114	4.84 ± 0.40	9.19
Sandtown	IIIAB	4.95 ± 0.10	3.396 ± 0.071	20.83 ± 0.32	21.32 ± 0.85	7.54
Schwetz	IIIAB	1.41 ± 0.03	1.025 ± 0.043	7.012 ± 0.145	12.40 ± 2.40	7.14
Sikhote-Alin	IIAB	1.37 ± 0.03	1.014 ± 0.032	7.300 ± 0.094	9.84 ± 0.66	5.62
Squaw Creek	IIAB	4.63 ± 0.09	3.262 ± 0.079	20.83 ± 0.33	17.41 ± 1.54	5.69
Tamentit	IIIAB	4.22 ± 0.08	2.929 ± 0.093	18.49 ± 0.24	19.74 ± 1.18	10.17
Trenton	IIIAB	2.56 ± 0.05	1.814 ± 0.046	13.39 ± 0.14	15.30 ± 0.71	7.91

Table A3. *Continued.* Radionuclide activities [dpm/kg] calculated from isotopic ratios measured by AMS and Ni concentrations (%).

Meteorite	Group	^{10}Be	^{26}Al	^{36}Cl	^{41}Ca	Ni
Treysa	IIIAB	4.66 ± 0.09	3.319 ± 0.068	20.29 ± 0.31	22.45 ± 1.81	8.63
Turtle River	IIIAB	5.29 ± 0.11	3.717 ± 0.098	22.16 ± 0.53	22.06 ± 0.88	9.16
Verkhne Udinsk	IIIAB	2.69 ± 0.05	1.159 ± 0.033	22.76 ± 0.50	0.080 ± 0.044	7.35
Zerhamra	IIIAB	3.79 ± 0.08	2.871 ± 0.096	18.60 ± 0.24	20.80 ± 1.14	8.77

The given uncertainties include the uncertainties from the AMS measurements and the blank corrections but not the uncertainties of the ^{10}Be, ^{26}Al, ^{36}Cl, and ^{41}Ca decay constants and the uncertainties of the carrier masses, the latter two are usually negligible. The uncertainties for the Ni concentrations are typically less than 1%. bdl = below detection limit, n.d. = not determined.

APPENDIX B
CORRECTING COSMOGENIC ^{10}Be AND ^{26}Al FOR CONTRIBUTIONS FROM SULFUR AND PHOSPHOROUS

The light cosmogenic nuclide concentrations in iron meteorites, for example, ^{10}Be, ^{26}Al, can be compromised by contributions from S and/or P. Consequently, ^{10}Be and ^{26}Al production rates not only depend on shielding but also on the trace element concentrations of the studied sample. Since the latter are usually not known, the interpretation of ^{10}Be and especially ^{26}Al production rates is notoriously difficult and sometimes unreliable. While we were able to correct contributions from S and P for the production of cosmogenic Ne isotopes, such corrections are not possible for ^{10}Be and ^{26}Al. A logical step would be to apply the results obtained from the Ne data also to ^{10}Be and ^{26}Al, that is, to assume that the degree of contamination determined from Ne also apply, with some scaling factors, to the radionuclides. This, however, is not correct. First, noble gases and radionuclides were determined on different aliquots. Second, the extraction procedure for noble gases, that is, total melting of the sample, likely degasses the metal together with the troilite and schreibersite inclusions. In contrast, the extraction procedure for the radionuclides is optimized to dissolve the metal; traces of troilite and schreibersite are very likely not be completely dissolved. Therefore, the S and P concentrations determined from cosmogenic Ne are expected to be higher than the ones for ^{10}Be and ^{26}Al. Despite being not entirely correct, we nevertheless use the results from Ne for correcting ^{26}Al.

Doing so, we apply the percentage of the correction used for ^{21}Ne also for ^{26}Al, that is, if we had to correct the ^{21}Ne data by 5%, we also correct the ^{26}Al data by 5%. The data for ^{10}Be are not corrected because the mass difference between ^{10}Be and S/P is much larger than the mass difference between ^{21}Ne or ^{26}Al and S/P. Consequently, the same contaminating level of S and/or P induces a significantly smaller contribution to ^{10}Be than it does for ^{21}Ne and ^{26}Al. The thus applied corrections for ^{26}Al are usually below 10%, exceptions are Charcas (correction factor 1.10), Sikhote-Alin (1.16), Boxhole (1.18), Piñon (1.25), Squaw Creek (1.27), Arispe (1.43), and Lombard (1.66). The ^{10}Be, ^{26}Al (corrected), and ^{36}Cl concentrations at the time of fall, that is, the production rates, are given in Table 2. The given uncertainties include the uncertainties of the measured radionuclide concentrations and the uncertainties of the terrestrial ages. For ^{26}Al, we added half of the value of the correction to the final uncertainties. For example, the ^{26}Al production rate for Avoca after correction for decay during terrestrial residence but before correcting for contributions from S and/or P is (3.06 ± 0.08) dpm kg^{-1}. After correction for contributions from S and/or P, the value reduces to 2.91 dpm kg^{-1}, that is, 0.15 dpm kg^{-1} is from S and/or P. We subsequently added half of this value, that is, 0.075 dpm kg^{-1} to the final uncertainties, that is, the final data are (2.91 ± 0.15) dpm kg^{-1} (Table 2). Production rates for ^{41}Ca are not given because they are no longer independent. Due to the way we calculated the terrestrial ages, ^{41}Ca production rates are simply given by 1.157 times the ^{36}Cl production rates.